

# Optimal Demodulation Domain for Microwave SQUID Multiplexers in Presence of Readout System Noise.

M. E. García Redondo,<sup>1,2,3,4</sup> N. A. Müller,<sup>1,5,3,4</sup> J. M. Salum,<sup>1,2,3,4</sup> L. P. Ferreyro,<sup>1,2,6,4</sup> J. D. Bonilla-Neira,<sup>1,5,6,4</sup> J. M. Geria,<sup>1,5,6</sup> J. J. Bonaparte,<sup>3,5,4</sup> T. Muscheid,<sup>2</sup> R. Gartmann,<sup>2</sup> A. Almela,<sup>1,3</sup> M. R. Hampel,<sup>1,3,6</sup> A. E. Fuster,<sup>1,3,6</sup> L. E. Ardila-Perez,<sup>2</sup> M. Wegner,<sup>2,5</sup> M. Platino,<sup>1,3,6,4</sup> O. Sander,<sup>2</sup> S. Kempf,<sup>5</sup> and M. Weber<sup>2</sup>

<sup>1</sup>*Instituto de Tecnologías en Detección y Astropartículas (ITeDA), Buenos Aires, Argentina*

<sup>2</sup>*Institute for Data Processing and Electronics (IPE), Karlsruhe Institute of Technology (KIT), Karlsruhe, Germany*

<sup>3</sup>*Comisión Nacional de Energía Atómica (CNEA), Buenos Aires, Argentina*

<sup>4</sup>*Universidad Nacional de San Martín (UNSAM), Buenos Aires, Argentina*

<sup>5</sup>*Institute of Micro- and Nanoelectronic Systems (IMS), Karlsruhe Institute of Technology (KIT), Karlsruhe, Germany*

<sup>6</sup>*Consejo Nacional de Investigaciones Científicas y Técnicas (CONICET), Buenos Aires, Argentina*

(\*Electronic mail: manuel.garcia@iteda.cnea.gov.ar.)

(Dated: 12 June 2024)

The Microwave SQUID Multiplexer ( $\mu$ MUX) is the device of choice for the readout of a large number of Low-Temperature Detectors in a wide variety of experiments within the fields of astronomy and particle physics. While it offers large multiplexing factors, the system noise performance is highly dependent on the cold and warm-readout electronic systems used to read it out, as well as the demodulation domain and parameters chosen. In order to understand the impact of the readout systems in the overall noise performance, first we extended the available  $\mu$ MUX simulation frameworks including additive and multiplicative noise sources in the probing tones (i.e. phase and amplitude noise), along with the capability of demodulating the scientific data, either in resonator's phase or amplitude. Then, considering the additive noise as a dominant noise source, the optimum readout parameters to achieve minimum system noise were found for both open-loop and flux-ramp demodulation schemes in the aforementioned domains. Later, we evaluated the system noise sensitivity to multiplicative noise sources under the optimum readout parameters. Finally, as a case study, we evaluated the optimal demodulation domain and expected system noise level for a typical Software-Defined Radio (SDR) readout system. This work leads to an improved system performance prediction and noise engineering based on the available readout electronics and selected demodulation domain.

## I. INTRODUCTION

Low-Temperature Detectors such as Transition-Edge Sensors (TES)<sup>1</sup>, Magnetic Microcalorimeters (MMC)<sup>2</sup> and Microwave Kinetic Inductance Detectors (MKID)<sup>3</sup> have demonstrated outstanding sensitivities in a large number of different experiments going from sub-mm/mm<sup>4</sup> and gamma/X-ray<sup>5</sup> astronomy to nuclear and particle physics<sup>6</sup>. Nowadays, current micro and nano-fabrication techniques allow to easily create focal planes populated with a huge number of detectors satisfying the requirements of the most demanding applications<sup>7</sup>. At the same time, multiplexing schemes that support these large detector counts are being developed in parallel in order to manage the system complexity and cooling requirements at sub-Kelvin stages where the detectors are operated<sup>8</sup>.

Along with the different multiplexing techniques developed for cryogenic detectors readout, a Frequency-Division Multiplexing (FDM) scheme that has become popular in the last decade is the Microwave Superconducting Quantum Interference Device (SQUID) Multiplexing ( $\mu$ MUXing)<sup>9,10</sup>. Its success lies in the available high channel carrying capacity and remarkable system scalability while maintaining the readout noise subdominant to the intrinsic detector noise<sup>11</sup>. This scheme encodes the detector signals in the resonance frequencies of multiple GHz-frequency superconducting resonators

coupled to a common feedline. Therefore, recovering the signals from each detector requires only monitoring the resonance frequencies. Despite these advantages, it places stringent requirements on the cold and warm readout systems responsible for generating and acquiring high-purity broadband microwave signals required to monitoring each channel.

In the case of single channel in-lab characterization and low-detector count experiments, the readout system noise is mainly dominated by the cryogenic Low-Noise Amplifier (LNA) in charge of recovering the low-power microwave signals coming out of the  $\mu$ MUX device<sup>10,12</sup>. This condition is achieved using bench-top instruments and expensive microwave components. On the other hand, high-count detectors readout and in-field measurements plans to use custom designed Software-Defined Radio (SDR) readout systems based on commercially available components with limited performance<sup>13-15</sup>. Therefore, the impact of the readout electronics becomes more relevant, especially in the readout of flux-transformer coupled devices such as Magnetic Microcalorimeters/bolometers<sup>16,17</sup> or with the introduction of near-quantum-limited amplification technologies such as parametric amplifiers<sup>18,19</sup>. As a consequence, it is important to have a software simulation framework which allows designers to predict the impact of these systems on the readout performance, as well as through its characterization, evaluate the

readout parameters that optimize the yield of a particular detection system.

Seeking to improve system noise predictions and find optimization parameters, we extended in this article the capabilities of the available simulation frameworks for the readout of Microwave SQUID Multiplexers<sup>20,21</sup> allowing to evaluate the impact of the cold and warm readout electronics systems in the overall readout performance. Previously developed frameworks solely consider additive noise, commonly attributed to the cryogenic LNA. However, characterizations performed over SDR readout systems unveil the presence of multiplicative noise<sup>15,22–24</sup>. These extra noise sources were included and their impact in the system performance was evaluated as a function of the readout parameters. Since the noise sources added act in different domains, the most commonly used demodulation domains, i.e. resonator's phase and amplitude, were also included.

This article is organized as follows: First, in section II we describe the  $\mu$ MUX model used for simulations and its dependence with flux and power. Second, section III presents the readout signal model adding additional noise sources attributed to the readout system and two demodulation schemes and domains are presented. Then, in section IV we show through simulations the minimum-noise readout parameters for additive noise in both demodulation schemes and evaluate the impact of the remaining noise sources under these conditions using a variety of different demodulation parameters. In addition, the impact of a typical SDR readout system is analyzed as an example. Finally, a discussion based on the obtained results is given in section V and the conclusions are presented in section VI.

## II. MICROWAVE SQUID MULTIPLEXER MODEL

Evaluating the readout performance of a  $\mu$ MUX under readout system noise first requires a model capable of replicating the complex underlying physics of superconducting resonators combined with the nonlinear behaviour of Josephson tunnel junctions. In this section we introduce the most important aspects of  $\mu$ MUX model that we will employ in section III. It is worth to mention that the main objective of this work is not to improve the current  $\mu$ MUX models, but rather to reuse the available ones<sup>21,25</sup> within a new simulation framework that includes new features and noise sources.

$\mu$ MUXing relies on High-Q superconducting microwave resonators as frequency encoding elements. Figure 1 shows a simplified schematic circuit diagram of a transmission line based  $\mu$ MUX. It comprises of a non-hysteretic current-sensing rf-SQUID inductively coupled to a superconducting quarter-wave transmission line resonator. The resonator, in turn, is capacitively coupled to a common feedline. Due to its Josephson parametric self-inductance, the rf-SQUID acts as a flux-dependent inductor allowing the resonance frequency modulation as a function of to the flux threading the SQUID loop, which is proportional to the detector signal coupled through the detector input coil. As a consequence, a probing tone injected at the multiplexer input (Left spectrum in figure 1) will

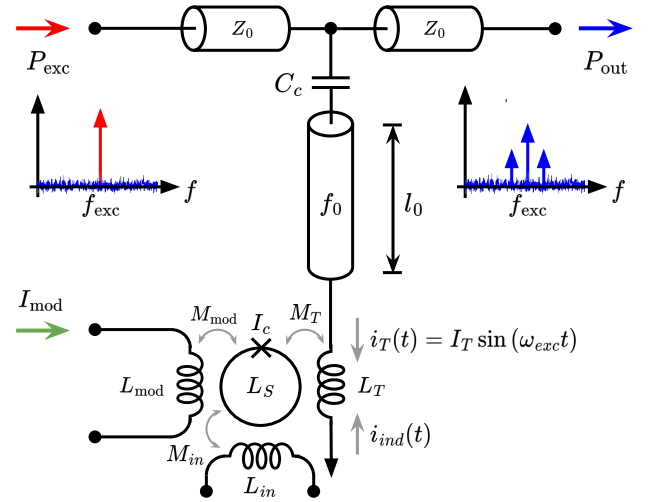


FIG. 1. Simplified schematic circuit diagram of a single readout channel of a transmission line based Microwave SQUID Multiplexer. Left) Probing tone spectrum with frequency  $f_{exc}$  and power  $P_{exc}$ . Right) Output tone spectrum with its modulation sidebands produced by the  $\mu$ MUX.

appear modulated in phase and amplitude at the multiplexer output (Right spectrum in figure 1). In this way, demodulating the output tones corresponding to each resonator allows us to decode the detector signals using a single pair of coaxial cables going in and out of the cryostat.

As in communications systems, noise performance depends on the modulation used, signal power and noise level. Accordingly, we will start describing the modulation produced by the  $\mu$ MUX in the probing tones. In the following subsection II A, we will present the resonance frequency flux and power dependence. Then in subsection II B, we will relate it with the resonator frequency response to finally in subsection III C introduce an example model that will be used in the next sections III and IV.

### A. Resonance Frequency Flux and Power Dependence

For the purpose of this work, we directly adopted the analytical  $\mu$ MUX readout power dependent model developed by Wegner<sup>25</sup> to describe the dependence of the resonance frequency as a function of the fluxes contributions threading SQUID loop  $f_r(\varphi)$ . This model assumes a finite Self-screening parameter  $\beta_L = 2\pi L_S I_c / \Phi_0$  as well as a non-zero readout available power  $P_{exc}$  at the  $\mu$ MUX input port with angular frequency  $\omega_{exc} = 2\pi f_{exc}$ . Under this condition, the supercurrent in the rf-SQUID can be written as,

$$I_S(t) = -I_c \sin \left[ \varphi_{mod} + \varphi_{exc} \sin(\omega_{exc} t) + \beta_L \frac{I_S(t)}{I_c} \right] \quad (1)$$

Where  $\varphi_{mod} = 2\pi M_{mod} I_{mod} / \Phi_0$  is a quasi-static magnetic

flux contribution induced by a current source  $I_{\text{mod}}$  coupled through  $M_{\text{mod}}$ ,  $\varphi_{\text{exc}} = 2\pi M_T I_T / \Phi_0$  is the amplitude of the time-variant magnetic flux induced by the probing tone through  $M_T$  and  $I_c$  the critical current of the Josephson junction. The term  $\varphi_{\text{scr}}(t) = \beta_L I_S(t) / I_c$  represents the self-screening flux. According to Lenz's law, a voltage  $u_{\text{ind}}(t) = -M_T dI_S(t)/dt$  is created which opposes the flux changes and hence the current  $i_{\text{ind}}(t)$  is induced in the resonator termination. Therefore, the total current at the resonator termination  $i_{\text{tot}}(t) = i_T(t) + i_{\text{ind}}(t)$  is a superposition of two contributions originating from the microwave probing tone and the supercurrent flowing through the SQUID loop. In this way, the total voltage across the resonator termination is  $u_{\text{ind}}(t) = L_T di_{\text{tot}}(t)/dt$  and can be expressed by introducing an effective termination inductance,

$$L_{T,\text{eff}} = L_T \frac{i_{\text{tot}}(t)}{i_T(t)} \quad (2)$$

Due to the transcendental nature of equation 1, there is no analytical solution for  $I_S(t)$  than can be directly inserted into equation 2. The required approximations and expansions of  $I_S(t)$  in order to obtain a useful expression for  $L_{T,\text{eff}}$  are described by Wegner<sup>25</sup>. The derived expression can be directly related to the circuit parameters shown in figure 1 yielding to the following resonance frequency expression as a function of the normalized fluxes  $f_r(\varphi_{\text{exc}}, \varphi_{\text{mod}})$ ,

$$f_r(\varphi_{\text{exc}}, \varphi_{\text{mod}}) \approx f_{\text{off}} + \frac{4f_0^2 M_T^2}{Z_0 L_S} \frac{2\beta_L}{\varphi_{\text{exc}}} \sum_{i,j} p_{i,j}(\varphi_{\text{exc}}, \varphi_{\text{mod}}) \quad (3)$$

Where  $f_{\text{off}} = f_0 - 4f_0^2(C_c Z_0 + L_T/Z_0)$  stands for the unaltered resonance frequency and  $p_{i,j} = a_{i,j} \beta_L^{b_{i,j}} J_1(c_{i,j} \varphi_{\text{exc}}) \cos(c_{i,j} \varphi_{\text{mod}})$  the Taylor expansion coefficients. Here,  $i$  denotes the expansion order and  $j$  the number of contribution of each order, while  $J_1$  is the order 1 Bessel function of the first kind. It is not the purpose of this article to derive the model equations in detail again, but to give the basic necessary elements to understand the following sections.  $p_{i,j}$  coefficients as well as a detailed analysis can be found in the following references<sup>25,26</sup>. The validity of this model sets an upper limit for  $\beta_L \leq 0.6$  and assumes a probing tone frequency  $f_{\text{exc}}$  close to the resonance frequency of the resonator  $f_r$ , leading to a maximum oscillating anti-node current amplitude  $I_T = \sqrt{\frac{16Q_l^2 P_{\text{exc}}}{\pi Q_c Z_0}}$ .  $Q_l$  and  $Q_c$  denote the loaded and coupling quality factors respectively, while  $Z_0$  is the characteristic impedance of both the resonator and the feedline.

## B. Frequency Response

The previously introduced expression can be inserted into the resonator transmission scattering parameter in order to

find the flux dependence of the resonator frequency response  $S_{21}(f_{\text{exc}}, \varphi)$ . Considering a perfectly symmetric lossy resonator<sup>21,27</sup> the analytical expression becomes,

$$S_{21}(f_{\text{exc}}, \varphi_{\text{exc}}, \varphi_{\text{mod}}) = \frac{S_{21}^{\text{min}} + 2jQ_l \left( \frac{f_{\text{exc}} - f_r(\varphi_{\text{exc}}, \varphi_{\text{mod}})}{f_r(\varphi_{\text{exc}}, \varphi_{\text{mod}})} \right)}{1 + 2jQ_l \left( \frac{f_{\text{exc}} - f_r(\varphi_{\text{exc}}, \varphi_{\text{mod}})}{f_r(\varphi_{\text{exc}}, \varphi_{\text{mod}})} \right)} \quad (4)$$

Here  $S_{21}^{\text{min}} \approx Q_l/Q_i$  represents the resonance depth,  $Q_l$  and  $Q_i$  are the loaded and intrinsic quality factors respectively. This equation describes a Lorentzian shaped frequency response, while in the complex plane follows a semi-circular trajectory with a center at  $x_c = (1 + S_{21}^{\text{min}})/2$  and radius  $r = 1 - x_c$  as can be seen in figure 2. This trajectory is approximately the same either for flux or frequency sweeps in the case of a negligible junction sub-gap resistance<sup>16,26</sup>. In the case of high quality resonators ( $Q_i \rightarrow \infty$ ), the bandwidth of the resonator can be easily approximated using  $BW_{\text{res}} \approx f_0/Q_l$ . Therefore,  $Q_l \approx Q_c$  and  $BW_{\text{res}}$  is only determined by the coupling through  $C_c$ . The symmetric frequency response described by equation 4 is a consequence of a good impedance matching between the resonator and the associated feed-line<sup>26,27</sup>.

## C. $\mu$ MUX Simulation Example

The  $\mu$ MUX analytical model described by equations 3 and 4 was numerically implemented using Python and tested with device parameters described in table I, that are typical for a  $\mu$ MUX device used in bolometric applications<sup>11</sup>. Using equation 3 the unaltered resonance frequency was calculated yielding  $f_{\text{off}} = 4.775$  GHz, while the peak-to-peak frequency shift  $\Delta f_r^{\text{mod}}$  for vanishing readout powers  $P_{\text{exc}} \rightarrow 0$  matches the resonator bandwidth  $BW_{\text{res}} \approx 200$  kHz. Since we commonly place the probing tone frequency  $f_{\text{exc}}$  close to the unaltered resonant frequency  $f_{\text{off}}$ , it is more convenient to express it in terms of the difference  $f_{\text{exc}} - f_{\text{off}}$  instead of its absolute frequency. We adopted this metric for our graphs in this work. Accordingly to the analytical model predictions at a power around  $P_{\text{exc}} \approx -64$  dBm the resonator became insensitive to the modulation flux  $\varphi_{\text{mod}}$ . For this reason, simulations performed in this work were limited to a power range between  $-90$  dBm and  $-60$  dBm.

It should be noted that the required condition of a probe tone frequency  $f_{\text{exc}}$  close to the resonance frequency  $f_r$  cannot be always satisfied, yielding to an overestimation of the radio-frequency flux induced within the SQUID when the probing tone is far away from it. In this case, an analytical calculation of  $I_T(f_{\text{exc}})$  cannot be found due to the recursive relation between  $f_r(\varphi_{\text{exc}})$  and  $\varphi_{\text{exc}}(f_r)$ . Therefore, we applied a similar solution that was used in previous articles<sup>21</sup>. But in this case,

the maximum value of the anti-node current  $I_T = \sqrt{\frac{16Q_l^2 P_{\text{exc}}}{\pi Q_c Z_0}}$  was scaled using narrow-band approximation of the transmission line resonator frequency response given by expression 4. This iterative process start in the condition of zero readout power  $P_{\text{exc}} \rightarrow 0$  to derive a first guess  $f_r^{i=0}$  and then executes

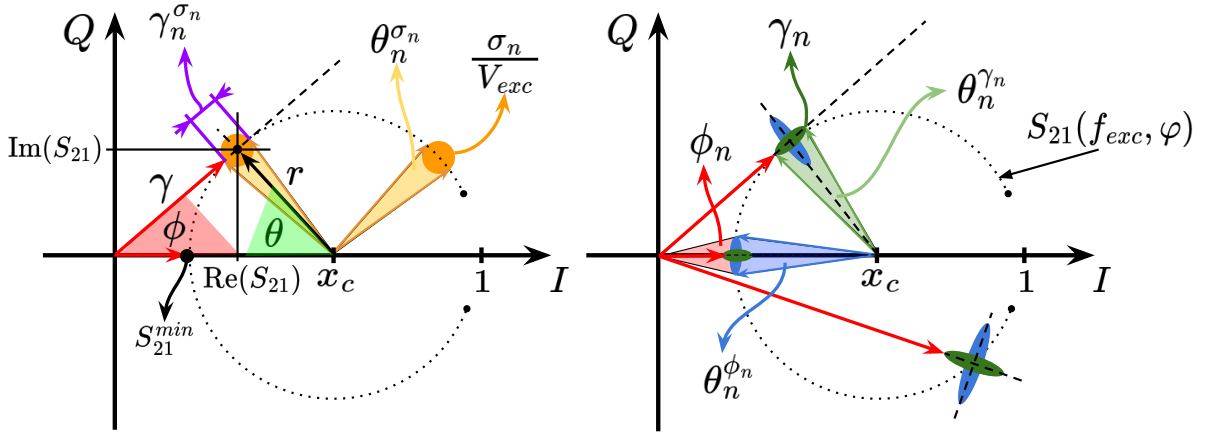


FIG. 2. Complex plane representation of the scattering parameter  $S_{21}(f_{\text{exc}}, \varphi)$  in its Canonical form, with the readout noise sources. Red arrows represent the normalized measured signal phasor with amplitude  $\gamma = |S_{21}|$  and phase  $\theta$ , while  $\phi$  is the resonator's phase measured from its rotating frame. Left) Additive source: Johnson–Nyquist noise  $\sigma_n(t)/V_{\text{exc}}$  represented as a circular orange noise cloud. Right) Multiplicative sources: Phase  $\phi_n(t)$  and Amplitude  $\gamma_n(t)$  noises represented with the blue and green ellipses respectively. The projection of each noise source into the resonator's phase and amplitude demodulation domains are denoted as:  $\gamma_n^{\sigma_n}(t)$ ,  $\theta_n^{\sigma_n}(t)$ ,  $\theta_n^{\phi_n}(t)$  and  $\theta_n^{\gamma_n}(t)$ . The superscript stands for the noise source that is being projected.

TABLE I.  $\mu\text{MUX}$  example parameters used during simulations. These are the typical design parameters for a  $\mu\text{MUX}$  optimized for bolometric applications<sup>11</sup>.

| Parameter        | Value  | Unit     |
|------------------|--------|----------|
| $f_0$            | 5      | GHz      |
| $Z_0$            | 50     | $\Omega$ |
| $L_S$            | 30     | pHy      |
| $L_T$            | 100    | pHy      |
| $\beta_L$        | 0.6    | -        |
| $M_T$            | 1.3    | pHy      |
| $M_{\text{mod}}$ | 20     | pHy      |
| $Q_i$            | 200000 | -        |
| $C_c^a$          | 5      | fF       |

<sup>a</sup>  $Q_c \approx (2\pi)/(2Z_0\omega_0C_c)^2$

the power dependent model sequentially using the previous results  $f_r^{i-1}$  until the equilibrium is reached or equivalently the convergence criteria is satisfied  $f_r^{i-1} \approx f_r^i + \varepsilon$ .

Due to the fact that in the next section we use a continuous-time analytical description, time-dependency was introduced considering a time varying modulation flux  $\varphi_{\text{mod}}(t)$ . The quasi-static flux condition imposed for equation 1 is fulfilled ensuring flux variations considerably slower than the resonator ring-down time  $\tau_{\text{down}} \approx 1/2\pi BW_{\text{res}}$  and consequently even slower than  $\tau_{\text{exc}} = 1/2\pi f_{\text{exc}}$ . This condition allowed the resonator to keep track of the flux variations while maintaining the steady-state frequency response<sup>21,28</sup> described by equation 4. Nevertheless, our model allows a first order approximation of the dynamic response by means of a low-pass filtered version of  $S_{21}$ . In order to simplify the nomenclature and facilitate the following analysis, we will only show explicitly the time dependence of the transmission parameter  $S_{21}(t)$  as a consequence of the flux variations  $\varphi(t)$ .

### III. READOUT SYSTEM MODEL

A simplified block diagram of the homodyne system used for the readout of a single  $\mu\text{MUX}$  channel is shown in figure 3. For the sake of simplicity, several of the microwave/RF components comprising the cold and the warm-temperature electronics were condensed into single blocks while preserving its functionality. The most important components of this system are: 1) A microwave synthesizer capable of generating the probing tone with frequency  $f_{\text{exc}}$ , and available power  $P_{\text{exc}}$  at the  $\mu\text{MUX}$  input port, 2) An arbitrary current waveform generator able to provide the required flux modulation  $\varphi_{\text{mod}}$  with frequency  $f_{\text{ramp}}$ , 3) The  $\mu\text{MUX}$  device described by the behavioural model explained in section II, 4) A set of noise sources representing all noise contributions attributed to the readout system (dashed red box), 5) Low-Noise amplification and filtering stages in charge to boost the signals and filter out unwanted components maintaining the Signal-to-Noise Ratio (SNR) and, 6) A complex IQ mixer that down-converts the signal in order to be processed later.

#### A. Measured Signals and Noise Sources

The complex base-band signal  $x(t) = x_I(t) + jx_Q(t)$  at the output of the homodyne readout system shown in figure 3 can be expressed as,

$$x(t) = G'V_{\text{exc}}S_{21}(t)m_n(t) + G'\sigma_n(t) \quad (5)$$

Where  $V_{\text{exc}} = \sqrt{2P_{\text{exc}}Z_0}$  is the amplitude of the probing tone, while  $\sigma_n(t)$  and  $m_n(t)$  are the additive and multiplicative noise terms respectively. Here, we consider an ideal IQ



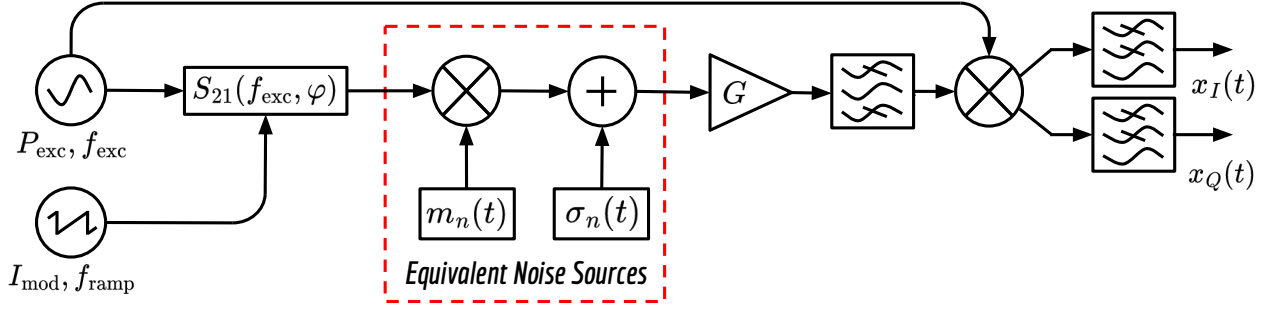


FIG. 3. Block diagram of the homodyne readout system used for the readout of a Microwave SQUID Multiplexer. From left to right) Microwave and arbitrary signal generators in charge of generating the probing tone and flux modulation,  $\mu$ MUX device, equivalent noise sources, low-noise amplifiers, filters and IQ mixer for signal conditioning and down-conversion. The noise sources inside the red rectangle  $\sigma_n(t)$ ,  $m_n(t)$  represent the additive and multiplicative noise sources attributed to the cold and warm readout system respectively and referred to the  $\mu$ MUX output.

mixer and a gain factor  $G' = Ge^{j\alpha}e^{2j\pi f_{exc}\tau}$  including the overall gain  $G$ , phase offset  $\alpha$  and time delay  $\tau$  added by the RF components and cables. In the context of a real measurement,  $G'$  can be determined during the calibration process or continuously monitored<sup>29</sup>. Therefore, for the purpose of this article we will assume that all of the aforementioned parameters are known and constant over time for the probing tone frequency  $f_{exc}$ . During the down-conversion process the time dependence of the excitation signal was removed keeping only the complex envelope of the modulated probing tone being equal to the scaled transmission parameter time-trace  $G'S_{21}(t)$ . When  $f_{exc}$  is located out of resonance, the transmission parameter is close to unity and the measured average signal amplitude approximately equals to  $x^{off}(t) \approx G'V_{exc}$ . This value can be used to define a normalized signal as,

$$\frac{x(t)}{x^{off}(t)} = S_{21}^{meas}(t) = S_{21}(t)m_n(t) + \frac{\sigma_n(t)}{V_{exc}} \quad (6)$$

Thus, the normalized signal is basically an estimation of the actual transmission parameter  $S_{21}(t)$ . Figure 2 shows the complex representation of  $S_{21}^{meas}$  where, as we mention in section II B and for the noise-less case, the measured signal (red arrow) describes a semi-circle centered at  $x_c$  with radius  $r$  as a consequence of a flux sweep. The  $|S_{21}^{meas}|$  takes values from  $S_{21}^{min}$  on resonance, to  $S_{21}^{min} \approx 1$  far out of resonance. Contrarily, in a real scenario represented by equation 5, noise sources produce a deviation from this trajectory that cannot be distinguished from the flux variations produced by the detector signal and are interpreted as a flux noise. In the next subsections we give a detailed description of the noise sources affecting the system in order to calculate the error in the transmission parameter determination and consequently derive the equivalent flux noise represented by each one. Since we want to analyze the impact of the readout system noise over different demodulation domains, we did not consider detector, SQUID and modulation flux noise sources.

### 1. Additive Sources

This type of noise refer to all kinds of noise sources that are directly added to the desired signals and remain even if the desired signal is not present. Considering the scope of this work, and based on previous articles<sup>19,21</sup>, we will only consider Johnson–Nyquist noise  $\sigma_n(t)$ . Johnson–Nyquist noise can be modeled as  $\sigma_n(t) = \sigma_I(t) + j\sigma_Q(t)$ , where real and imaginary components are both zero-mean, finite power, Independent and Identically Distributed (IID) Gaussian random variables. A normalized version  $\sigma_n(t)/V_{exc}$  can be seen as an orange circular noise cloud in figure 2. This model is well suited to describe a wide range of noise sources present in readout electronics systems such thermal, electric or quantization. In a properly designed system, the additive noise is typically dominated by the cryogenic High-Electron Mobility Transistor (HEMT) amplifier<sup>12</sup>. Because of their importance, many groups are actively trying to improve them or even replace them with new amplification technologies such as quantum-limited parametric amplifiers<sup>18,19</sup>. While these new technologies represent an important reduction of the additive noise level, they make evident the presence of other types of sources such as those we describe below. Additionally to the Johnson–Nyquist noise, spurious signals generated by the electronics<sup>15</sup> can be also included as additive interferences, but for the scope of this work they will not be included because unlike noise, they are localized in frequency and can be mitigated<sup>30</sup>.

### 2. Multiplicative Sources

Contrary to additive sources, multiplicative noise sources depend on the presence of the desired signal. Their level depend on the signal strength and mathematically, as the name implies, the noise is multiplied with the desired signal  $S_{21}(t)$  as,

$$m_n(t) = [1 + \gamma_n(t)]e^{j\phi_n(t)} \quad (7)$$

Here, we will only focus on amplitude  $\gamma_n(t)$  and phase  $\phi_n(t)$  noise which are the most common multiplicative noise sources present in readout electronics systems<sup>31,32</sup>. Both are real random variables described by their auto-correlation function as we will explain in subsection III B. Both are real random variables described by their auto-correlation function as we will explain in subsection III B. A simplified and magnified representation of these noises using colored ellipses is shown in the right side of figure 2. The term  $\gamma_n(t)$  represents small signal variations (green ellipses) parallel to the measured signal amplitude (red arrow), while  $e^{j\phi_n(t)}$  as perpendicular signal variations (blue ellipses). Due to their multiplicative nature, when the measured signal amplitude decreases (i.e., at resonance), the voltage fluctuations decrease proportionally, keeping the amplitude and phase variations constant. Traditionally, amplitude and phase noise are terms used to describe short-term variations or instabilities, with "short-term" referring to time intervals on the order of seconds or less<sup>33</sup>. These are commonly generated when some system parameter randomly fluctuates (e.g. due to thermal or flicker noise) translating that variation to the desired signal. This process called parametric up-conversion does not differ to much from the  $\mu$ MUX working principle where the resonance frequency (system parameter) is modulated proportionally to the detector signal. This is the reason why the interest of this work is focused on including these noise sources and evaluating their impact on the system noise.

Besides being focused on noise sources generated by the readout system, this manuscript additionally includes the Two-Level System Noise. The evidence suggest that this noise is caused by Fluctuating Two-Level Systems (TLS) in dielectric materials, either the bulk substrate or its exposed surface, the interface layers between the metal films and the substrate, or any oxide layers on the metal surfaces that comprises the transmission line resonator<sup>34,35</sup>. This noise affects the distributed capacitance and therefore produces fluctuations in the resonance frequency that are seen as rotations of the resonance circle around its center. As well as amplitude noise in equation 7, it can be expressed as frequency fluctuations  $f_r \cdot f_{\text{TLS}}(t)$  around the unaltered resonance frequency  $f_{\text{off}}$ .

$$f_r(t) = f_r[1 + f_{\text{TLS}}(t)] \quad (8)$$

Although TLS noise is not generated by the readout electronics, it can act differently depending on the demodulation domain and readout parameters as well as the readout noise sources. This is why its impact will be also evaluated.

## B. Noise Metrics

Due to its random nature, noise is analyzed as a stochastic process. For wide-sense-stationary and ergodic random process  $y(t)$ , the Wiener-Khinchin theorem says that a power spectral density can be defined in terms of the Fourier transform of the statistical expected value, e.g. the auto-correlation<sup>31</sup> function as follows,

$$S_y(\Delta f) = \mathcal{F} \{R_{yy}(\tau)\} = \mathcal{F} \{y(0), y(\tau)\} \quad (9)$$

Thus, spectral features of noise are entirely determined by the Noise Spectral Density  $S_y(\Delta f)$  (NSD). The requirement that noise be stationary and ergodic are the equivalent of "repeatable" and "reproducible" in experimental physics. In our case,  $S_y(\Delta f)$  is the base-band representation of the NSD measured at a frequency offset  $\Delta f$  from the probing tone frequency  $f_{\text{exc}}$ . For the case of Johnson–Nyquist noise, the statistic independence implies white noise with constant NSD equals to  $S_N = k_B T_n$ , where  $T_n$  is the so called noise temperature and  $k_B$  the Boltzmann's constant. Therefore, the NSD of the normalized Johnson–Nyquist noise respect to the probing tone amplitude  $\sigma_n(t)/V_{\text{exc}}$  is,

$$S_{\sigma_n}(\Delta f) = \frac{k_b T_n}{P_{\text{exc}}} \quad (10)$$

This quantity is usually expressed in dBc/Hz and  $T_n$  is the noise equivalent temperature referred to the  $\mu$ MUX output. In the context of this work, we will distinguish between  $T_n$  and  $T_{\text{sys}}$  due to the fact that  $T_{\text{sys}}$  is commonly experimentally determined and as we will see later, corresponds to an equivalent noise temperature that takes into account all the different noise sources acting simultaneously and producing the same system noise level<sup>19</sup>.

On the other hand, amplitude, phase or TLS noise exhibits certain degree of correlation between realizations yielding to colored noise spectral densities. They are commonly described by power law as,

$$S_y(\Delta f) = \sum_n b_n(\Delta f)^n \quad (11)$$

With values of  $n = [-4, 0]$  for phase,  $n = [-2, 0]$  for amplitude<sup>31</sup> and  $n = [-1, -1/2]$  for TLS<sup>34</sup>. As in the case of Johnson–Nyquist, phase and amplitude noise are expressed in dBc/Hz and represent the noise power integrated in a 1-Hz bandwidth at a  $\Delta f$  offset from  $f_{\text{exc}}$  relative to the probe tone power. In the TLS case, it is expressed in fractional frequency fluctuations  $S_{f_r}(f)/f_r^2$  in units of  $\text{Hz}^{-1}$ . Opposed to uncorrelated sources, depending on the degree of correlation, noise can be removed. This is the case of phase noise in radio systems which use different oscillators and clocks locked to the same frequency reference during up-and down-conversion processes as well as during generation and sampling. Therefore,  $\phi_n(t)$  used in equation 7 stands for the so-called "residual" phase noise<sup>32</sup>. Due to the fact that is a multiplicative quantity it can be arbitrarily referred to any part of the circuit yielding the same behaviour.

## C. Readout System Example

As an example, figure 4 shows residual amplitude and phase noise spectral densities for a Direct-RF Software-Defined Radio (SDR) readout system based on the RFSoc ZCU216

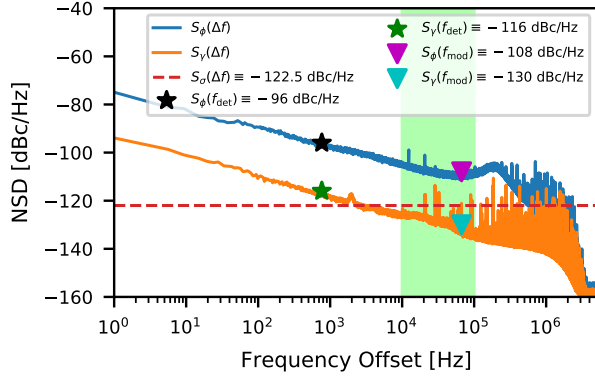


FIG. 4. Noise spectral densities for typical cold and warm-temperature readout systems at a frequency of  $f_{\text{exc}} = 5.5$  GHz. Blue and orange solid lines are the residual phase and amplitude noise spectral densities. Dashed red line is the additive NSD calculated with equation 10 using an equivalent noise temperature of a  $T_n = 4$  K, and probing power  $P_{\text{exc}} = -70$  dBm. Black and green stars represent phase and amplitude noise measured at  $f_{\text{det}} \approx 762$  Hz. The green region covers the possible modulation frequencies  $f_{\text{mod}}$  where the signal of interest is typically located in the case of bolometric applications<sup>15</sup>. Particularly, we used  $f_{\text{mod}} \approx 62$  kHz where phase and amplitude noise takes values represented by magenta and cyan triangles respectively.

evaluation kit<sup>36</sup>. These measurements were taken at a frequency of  $f_{\text{exc}} = 5.5$  GHz using a loop-back cable connecting transmitter (Tx) and receiver (Rx) ensuring that most of the coherent noise is removed in the down-conversion/sampling process<sup>15</sup>. A power sweep was performed until the amplitude and phase spectra reached power-independent values consistent with the nature of the multiplicative noise. At frequency offsets below 10 kHz amplitude and phase noise densities have  $-10$  dB/decade slopes demonstrating the colored behaviour described by equation 11, while the roll-off at frequencies above 1 MHz is due to the low-pass filter applied during signal channelization. In contrast with the multiplicative sources, the additive noise spectral density which is expected to be dominated by the cold readout system was theoretically calculated using equation 10, assuming a  $T_n = 4$  K and probing power  $P_{\text{exc}} = -70$  dBm yielding to  $S_{\sigma}(\Delta f) \approx -122.5$  dBc/Hz. The noise values shown in figure 4 will be used in the last section along with the  $\mu\text{MUX}$  model (table I) with the goal of estimating the readout noise performance.

After all noise sources and metrics were introduced and an example was given, the error term in the determination of the transmission scattering parameter as a function of time  $S_{21}(t)$  can be written as,

$$\delta S_{21}(t) = S_{21}(t) \gamma_n(t) e^{j\phi_n(t)} + \frac{\sigma_n(t)}{V_{\text{exc}}} \quad (12)$$

In the next section we will introduce the two most widely used demodulation domains and analyze the projection of the error term  $\delta S_{21}(t)$  on them in order to evaluate the demodula-

tion performance.

#### D. Demodulation Domains and Schemes

Slow variations in the flux, given either by a modulation  $\phi_{\text{mod}}(t)$  or a detector  $\phi_{\text{det}}(t)$ , lead to variations of the resonator frequency response as described by equation 4 and depicted in figure 2. The most widely used domains in which these variations are demodulated are: 1) The resonator's phase measured from its rotating frame<sup>19,37,38</sup> and 2) The amplitude of the transmission scattering parameter<sup>21,39</sup>. Both are respectively defined as,

$$\theta(f_{\text{exc}}, \varphi) = \arctan \left\{ \frac{\text{Im}[S_{21}(f_{\text{exc}}, \varphi)]}{x_c - \text{Re}[S_{21}(f_{\text{exc}}, \varphi)]} \right\} \quad (13)$$

$$\gamma(f_{\text{exc}}, \varphi) = |S_{21}(f_{\text{exc}}, \varphi)| \quad (14)$$

A representation of both domains is shown on the left of figure 2. While both domains are used showing outstanding performance, there is not an available simulation framework that allows to compare their performance in the presence of readout system noise, especially multiplicative. Using equations 13 and 14 we are able to define the projection of the error term  $\delta S_{21}(t)$  in both domains. Thus,  $\theta_n^{\sigma_n}(t)$ ,  $\gamma_n^{\sigma_n}(t)$  correspond to resonator phase and amplitude error due to additive noise  $\sigma_n(t)$ , while  $\theta_n^{\phi_n}(t)$  and  $\theta_n^{\gamma_n}(t)$  correspond to the resonator phase error due phase  $\phi_n(t)$  and amplitude  $\gamma_n(t)$  noise respectively. Unlike the rest, amplitude noise  $\gamma_n(t)$  is already projected into the amplitude domain by definition. These projections are depicted in figure 2 using shaded yellow, green, red and blue triangles. In the condition of small noise amplitudes, the geometrical projection of each noise source into the different domains can be calculated and the NSD derived yielding the analytical expressions shown in table II. A detailed analysis of these derivations be found in appendix A. The dependence of the NSD with  $f_{\text{exc}}$ ,  $\varphi$  and  $\Delta f$  was removed in order to avoiding a complex notation.

Expressions in table II corresponding to additive noise represent the easiest cases to analyze because it describes a constant radius noise cloud independent of the trajectory described by the resonator's response. Therefore, its projections either in resonator's phase or amplitude are constant. Conversely, multiplicative noise projections depend on the position in the resonance circle  $S_{21}(f_{\text{exc}}, \varphi)$  in which they are calculated (i.e. amplitude  $\gamma$ , readout phase  $\phi$  and resonator phase  $\theta$ ). Particularly in these cases can be a condition for minimum or zero projection depending on the readout domain and readout parameters chosen. For example, in the case of readout amplitude noise  $\gamma_n(t)$  there is no projection into the resonator phase domain when the readout phasor (red arrow in figure 2) is parallel to the circle radius ( $\theta + \phi = 0$ ). In contrast for readout phase noise  $\phi_n(t)$ , there is no projection into the resonator phase domain when the readout phasor is tangent to the resonance circle ( $\theta + \phi = \pi/2$ ). In addition, using the

TABLE II. . Spectral densities of additive and multiplicative noise sources projected in both demodulation domains.  $S_\theta$  represents the flux spectral density in resonator's phase readout while  $S_\gamma$  in amplitude. The dependence of the parameters with  $f_{exc}$ ,  $\varphi$  and  $\Delta f$  was removed in order to avoiding a complex notation.

| Readout Domain | Additive Noise $\sigma_n$               | Amplitude Noise $\gamma_n$                            | Phase Noise $\phi_n$                                |
|----------------|---|---|---|
| $S_\theta$     | $\frac{1}{r^2} \frac{k_B T_n}{P_{exc}}$ | $\frac{\gamma^2 \sin^2(\phi + \theta)}{r^2} S_\gamma$ | $\frac{\gamma^2 \cos^2(\phi + \theta)}{r^2} S_\phi$ |
| $S_\gamma$     | $\frac{k_B T_n}{P_{exc}}$               | $\gamma^2 S_\gamma$                                   | –   |

expressions in table II we conclude that additive noise is the dominant noise due to the fact that when considering equal noise densities (i.e.  $S_\gamma = S_\phi = \frac{k_B T_n}{P_{exc}}$ ), multiplicative sources are scaled by factors lower than unity respect to the additive. Despite these expressions allowing us to calculate resonator's phase and amplitude noise projections, an additional step is required in order to convert them to flux noise for a later comparison. This step depends on the demodulation scheme used and will be explained below.

### 1. Open-Loop Demodulation

When a detector signal is coupled to the SQUID through the input coil  $L_{in}$  (see figure 1), it creates a flux component  $\varphi_{det}(t)$  that is added to the modulation flux  $\varphi_{mod}(t)$ . For a given constant  $f_{exc}$ ,  $P_{exc}$ , and flux  $\varphi_{mod}$ , small flux variations  $\delta\varphi_{det}(t)$  will lead to resonator's phase  $\theta(t)$  and amplitude  $\gamma(t)$  variations described by,

$$\theta(t) \approx \delta\varphi_{det}(t) \left. \frac{\partial\theta}{\partial\varphi} \right|_{f_{exc}, P_{exc}, \varphi_{mod}} \quad (15)$$

$$\gamma(t) \approx \delta\varphi_{det}(t) \left. \frac{\partial\gamma}{\partial\varphi} \right|_{f_{exc}, P_{exc}, \varphi_{mod}} \quad (16)$$

This readout scheme is called open-loop and the demodulated signals  $\theta(t)$  and  $\gamma(t)$  are scaled copies of  $\delta\varphi_{det}(t)$ . The scaling factors are denoted as open-loop gains, or transfer coefficients equivalently, being equal to the partial derivatives of the corresponding demodulation domain with respect to the normalized flux evaluated at  $f_{exc}$ ,  $P_{exc}$  and  $\varphi_{mod}$ . Consequently, the maximum demodulated signal amplitudes are obtained when the maximum partial derivatives are achieved. Figure 5 shows the simulated resonator's phase (top) and amplitude (bottom) derivatives for the  $\mu$ MUX model described in section I as a function of the modulation flux  $\varphi_{mod}$  and probing tone frequency  $f_{exc}$  for a specific probing power  $P_{exc} = -70$  dBm. The absolute maximum gain for the resonator's phase  $G_\theta^{opt}$  is represented by the blue star, while upper  $G_\gamma^{opt,up}$  and lower  $G_\gamma^{opt,low}$  local maximum open-loop gains with black and cyan stars respectively.

These gain factors allow us to calculate the resonator's phase and amplitude variations, but also can be used in the reverse way to derive the equivalent flux change for given resonator phase and amplitude variations. Therefore, the NSD of

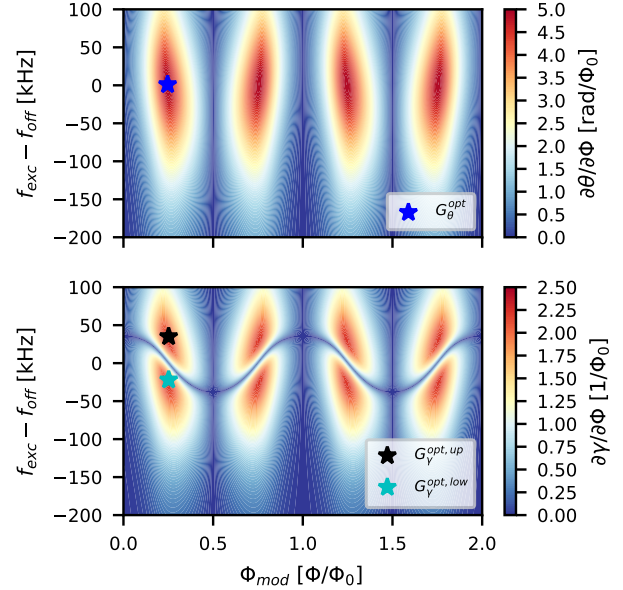


FIG. 5. Open-loop gains corresponding to the  $\mu$ MUX model presented in table I as a function of probe frequency  $f_{exc}$  and modulation flux  $\varphi_{mod}$  for a constant probing power  $P_{exc} = -70$  dBm. Top) Resonator's phase gain, black star represents the maximum gain  $G_\theta^{opt}$ . Bottom) Amplitude gains, black and cyan stars represent the both upper  $G_\gamma^{opt,up}$  and lower  $G_\gamma^{opt,low}$  local maximum gains.

the noise projections listed in table II can be translated into an equivalent flux noise density for resonator's phase  $\sqrt{S_\Phi^\theta}$  and amplitude  $\sqrt{S_\Phi^\gamma}$  readout using,

$$\sqrt{S_\Phi^\theta} \approx \sqrt{S_\theta(\Phi)} \left| \frac{\partial\theta(\Phi)}{\partial\Phi} \right|^{-1} \quad (17)$$

$$\sqrt{S_\Phi^\gamma} \approx \sqrt{S_\gamma(\Phi)} \left| \frac{\partial\gamma(\Phi)}{\partial\Phi} \right|^{-1} \quad (18)$$

Simplifying the notation for reading purposes, the dependence of the noise projection with probing frequency and power was avoided only preserving the explicit dependence with the magnetic flux  $\Phi$ . A similar expression for the flux noise  $\sqrt{S_\Phi^{TLS}}$  can be found for TLS noise<sup>10,26</sup>. Since it acts

directly in the resonance frequency, it can be related with the flux using,

$$\sqrt{S_{\Phi}^{TLS}} \approx \sqrt{S_{f_r}} \left| \frac{\partial f_r(\Phi)}{\partial \Phi} \right|^{-1} \quad (19)$$

Where  $\frac{\partial f_r(\Phi)}{\partial \Phi}$  is the derivative of equation 3 with respect to the flux and  $\sqrt{S_{f_r}}$  the frequency NSD. Although it is experimentally possible to determine the optimum flux bias necessary to obtain the maximum transfer coefficients, one of the main disadvantages of this scheme is that the information lies in the modulation side-bands located at a frequency offset equal to  $f_{det}$  where generally the phase  $S_{\gamma}(f_{det})$ , amplitude  $S_{\phi}(f_{det})$  and TLS  $S_{f_r}(f_{det})$  noise sources are considerably large compared with Johnson–Nyquist noise  $\frac{k_B T_n}{P_{exc}}$  as it can be seen in figure 4 represented with green and black stars. Therefore, special care should be given to multiplicative and TLS noise sources in the case of bolometric applications where the detector signal is extremely slow and faint<sup>11,17</sup> or a different readout method to overcome this problem need to be used.

## 2. Flux-Ramp Demodulation

In addition to the aforementioned problem, random flux offsets trapped inside the SQUID loop would require individual flux tuning of every channel in order to achieve the maximum open-loop gain, re-introducing the multiplexing problem. A technique called Flux-Ramp Modulation<sup>28</sup> (FRM) was introduced as a solution to overcome this limitation. On it, a common flux line is shared among all SQUIDS and a sawtooth-shaped flux with amplitude  $M_{mod} I_{mod} = n_{\Phi_0} \Phi_0$  and reset frequency  $f_{ramp}$  is applied sweeping all the possible operating points (see upper plot in figure 6). Due to the SQUID periodic response, resonator phase  $\theta(t)$  and amplitude  $\gamma(t)$  will have the same periodicity equal to  $f_{mod} = n_{\Phi_0} f_{ramp}$ . Therefore, a considerably slow detector signal  $\varphi_{det}(t)$  added to the the sawtooth-shaped modulation can be seen as a phase modulation, where  $\varphi_{det}(t)$  determines the instantaneous phase changes of the periodic responses (middle plot in figure 6). As a consequence of FRM, detector information in up-converted to the frequency  $f_{mod} = n_{\Phi_0} f_{ramp}$  (green region in figure 4) avoiding in this way noise levels close to the probe tone frequency  $f_{exc}$ . However, an additional phase demodulation step is required in order to recover the detector signal (Flux-Ramp Demodulation or FRD). In the context of this article we will analyze the flux demodulation noise performance using the linearity-improved quadrature demodulation<sup>40</sup>. The demodulated flux for the resonator phase  $\theta(t)$ , and amplitude  $\gamma(t)$  demodulation can be written respectively as,

$$\varphi_{\theta}(t') = \arctan \left[ \frac{\int \sin(2\pi p f_{mod} t) w(t) \theta(t) dt}{\int \cos(2\pi p f_{mod} t) w(t) \theta(t) dt} \right] \quad (20)$$

$$\varphi_{\gamma}(t') = \arctan \left[ \frac{\int \sin(2\pi p f_{mod} t) w(t) \gamma(t) dt}{\int \cos(2\pi p f_{mod} t) w(t) \gamma(t) dt} \right] \quad (21)$$

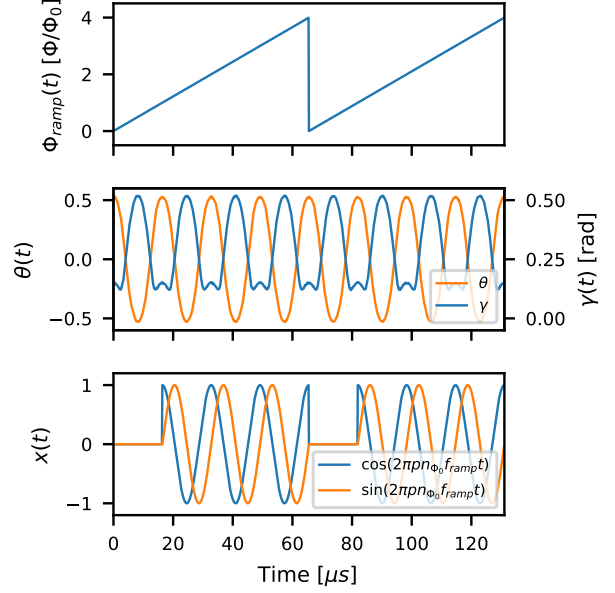


FIG. 6. Signals associated with the flux-ramp demodulation process of the  $\mu$ MUX model presented in table I for a particular  $f_{exc}$  and  $P_{exc}$ . Top) Flux-Ramp Modulation signal spanning  $n_{\Phi_0} = 4$  with  $f_{ramp} \approx 15.25$  kHz. Middle) Resonator's phase and amplitude signals before FRD. Bottom) Reference signals used for demodulation including the discarded period  $n_{disc} = 1$  and using the first harmonic component  $p = 1$ .

Here,  $w(t)$  accounts for both the discarding window, where a number of SQUID periods  $n_{disc}$  is set to zero avoiding the sawtooth-shaped flux non-ideal transition and the window function used to attenuate the non-linearity components. An integer number  $p$  is added allowing the demodulation of higher order FRM harmonics as we will use later in section IV B 1. The bottom part of figure 6 shows the cosine and sine reference signals used for FRD. Particularly in this example one of a total of four periods is discarded and a boxcar window is used. In this scheme, the integration is performed over a flux-ramp period setting an effective sampling rate of  $f_{ramp}$ . Here, we use continuous time notation for explanatory purposes and  $t'$  to explicitly show this implicit decimation.

In contrast with open-loop demodulation, FRM sweeps all the possible flux values varying the open-loop gains from its maximum and minimum values. As a consequence, equations 18 and 17 need to be integrated over a one flux-ramp period in order to get the demodulated noise level. As a natural solution, a gain-weighted average noise value may be used, but expressions 17, 18 and 19 diverge in the case of zero gain. For this reason, traditionally a Root-Mean-Square (RMS) gain over a flux-ramp period is defined<sup>21,28</sup> and flux noise density in the case of resonator's phase and amplitude is calculated using,

$$\sqrt{S_{\Phi}^{\theta}} \approx \sqrt{S_{\theta}} \left\{ \frac{1}{n_{\Phi_0} \Phi_0} \int_{n_{disc} \Phi_0}^{n_{\Phi_0} \Phi_0} \left( \frac{\partial \theta(\Phi)}{\partial \Phi} \right)^2 d\Phi \right\}^{-1} \quad (22)$$



$$\sqrt{S_{\Phi}^{\gamma}} \approx \sqrt{S_{\gamma}} \left\{ \frac{1}{n_{\Phi_0} \Phi_0} \int_{n_{\text{disc}} \Phi_0}^{n_{\Phi_0} \Phi_0} \left( \frac{\partial \gamma(\Phi)}{\partial \Phi} \right)^2 d\Phi \right\}^{-1} \quad (23)$$

Similarly for TLS, a flux noise density can be calculated as well,

$$\sqrt{S_{\Phi}^{\text{TLS}}} \approx \sqrt{S_{f_r}} \left\{ \frac{1}{n_{\Phi_0} \Phi_0} \int_{n_{\text{disc}} \Phi_0}^{n_{\Phi_0} \Phi_0} \left( \frac{\partial f_r(\Phi)}{\partial \Phi} \right)^2 d\Phi \right\}^{-1} \quad (24)$$

Where expressions between brackets are the gain-mean squares over a flux-ramp period and  $S_{\theta}$ ,  $S_{\gamma}$  and  $S_{\text{TLS}}$  are evaluated at  $f_{\text{mod}}$ . Due to the fact that we are discarding  $n_{\text{disc}}$  periods of a total of  $n_{\Phi_0}$  and applying a window function, we expect a degradation equal to  $\sqrt{\kappa/\alpha}$ , where  $\alpha = (n_{\Phi_0} - n_{\text{disc}})/n_{\Phi_0}$ . A  $\kappa$  factor was added to account for the degradation caused by the window applied. When boxcar window is used  $\kappa = 1$ . While these expressions give a rough estimation of the noise level, they have several limitations that this work aims to overcome. Unlike additive and TLS noise, these expressions do not apply to the case of multiplicative noise where both spectral densities and gains are flux dependent (i.e.  $\sqrt{S_{\theta, \gamma}(\Phi)}$ ). Another limitation is that due to the non-sinusoidal resonator's phase and amplitude responses, the information is not only contained in a single side-band, but spread out in harmonics of  $f_{\text{mod}}$  which cannot be demodulated using the quadrature demodulation method. Additionally, an extra challenge lies in the analytical calculation of the derivatives with respect to the flux, for the given conditions of readout power and frequency using the model presented in section II and their integration over a flux-ramp period. Especially when multidimensional optimization criteria must be found. That is why in this work the evaluation of the optimal readout parameters that match the lowest noise condition in both domains and demodulation methods will be performed by means of numerical simulations.

#### IV. SYSTEM NOISE SIMULATION

In this section we present several simulations performed in order to evaluate the demodulated noise for different readout conditions. Previously, for sake of simplicity a continuous-time signal model of the readout system was introduced. From now on, we will migrate to its discrete-time equivalent using adequate sampling frequency  $f_s$  that satisfies the sampling theorem. This migration is not only motivated by the numerical simulation, but also because the demodulation is typically done in the digital domain using Software-Defined Radio (SDR) Systems<sup>39,41</sup>. The readout system simulation framework was implemented completely in Python and making use of several available libraries. Table III enumerates the parameters used in the following simulations.

The general simulation procedure to obtain a demodulated signal time-trace can be summarized as follows:

TABLE III. Readout system parameters used during demodulated noise simulations.

| Parameter             | Value            | Unit       |
|-----------------------|------------------|------------|
| $f_s$                 | $\approx 7.82$   | MHz        |
| $N_s$                 | $2^{20}$         | Samples    |
| $BW_{\text{readout}}$ | 2                | MHz        |
| $f_{\text{det}}$      | $\approx 762.90$ | Hz         |
| $A_{\text{det}}$      | 1                | m $\Phi_0$ |
| $f_{\text{ramp}}$     | $\approx 15.25$  | kHz        |
| $n_{\Phi_0}$          | 4                | -          |
| $n_{\text{disc}}$     | 1                | -          |
| $p$                   | 1                | -          |
| $w[n]$                | Hamming          | -          |

1. The total modulation flux  $\varphi_{\text{tot}}[m]$  is created adding the modulation flux  $\varphi_{\text{mod}}[m]$  to the detector flux  $\varphi_{\text{det}}[m]$ .
2. Given fixed  $f_{\text{exc}}$  and  $P_{\text{exc}}$ ,  $f_r[m]$  is iteratively calculated using equation 3 and  $f_{\text{TLS}}[m]$  is added.
3. Then,  $S_{21}[m]$  is calculated through equation 4 for a particular  $f_{\text{exc}}$ , low-pass filtered and the readout noise sources  $\sigma_n[m]$ ,  $\phi_n[m]$  and  $\gamma_n[m]$  included.
4. Finally, and after a new step of signal conditioning,  $\theta[m]$  and  $\gamma[m]$  are available to be demodulated using some of the methods presented in previous section.

#### A. Open-Loop Demodulation Noise Performance

Using our simulation framework, we replicated the measurement process that is carried out in the laboratory during characterization. This allowed us to not only evaluate the noise performance, but also to know the required functionalities of our SDR readout system. For the determination of the noise density in the open-loop scheme described by equations 17 and 18, we must know the value of the open-loop gains (transfer coefficients) which depend on the readout frequency  $f_{\text{exc}}$  and power  $P_{\text{exc}}$  as well as the applied constant modulation flux  $\varphi_{\text{mod}}$ . First, for each value of frequency and power, one period of the transmission scattering parameter  $S_{21}(f_{\text{exc}}, P_{\text{exc}}, \varphi_{\text{mod}})$  was calculated sweeping  $\varphi_{\text{mod}}$ . Then, we get resonator's phase  $\theta(f_{\text{exc}}, P_{\text{exc}}, \varphi_{\text{mod}})$  and amplitude  $\gamma(f_{\text{exc}}, P_{\text{exc}}, \varphi_{\text{mod}})$  to consequently obtain the partial derivatives with respect to flux as can be seen in figure 5. For the next process, we stored the maximum gains  $G_{\theta}^{\text{opt}}(f_{\text{exc}}, P_{\text{exc}})$  and  $G_{\gamma}^{\text{opt}}(f_{\text{exc}}, P_{\text{exc}})$  along with the correspondent fluxes  $\varphi_{\text{mod}}^{\text{opt}}$  and resonance circle parameters (i.e. radius  $r$  and center  $x_c$ ). Resonance circle parameters determine the rotating frame required to calculate the resonator's phase using equation 13 when detector signal is present. This calibration procedure allows us to get all parameters required to obtain a demodulated signal time-trace.



### 1. Optimum Readout Parameters for Open-Loop

In order to find the optimum readout parameters, for each frequency  $f_{\text{exc}}$  and power  $P_{\text{exc}}$ , a small detector signal  $\varphi_{\text{det}}[m]$  was added to the fluxes corresponding to the maximum gains  $\varphi_{\text{mod}}^{\text{opt}}$ . The transmission parameter calculated and the readout noise sources included. Consequently, depending on the selected domain, resonator's phase  $\theta[m]$  and amplitude  $\gamma[m]$  time-traces calculated and  $\varphi_{\theta}[m]$  and  $\varphi_{\gamma}[m]$  derived dividing them by their correspondent optimum open-loop gain coefficients. By means of the Welch's method<sup>42</sup>, the white flux noise spectral density  $\sqrt{S_{\Phi, \text{white}}}$  was calculated. The results of these simulations for both domains are shown in figure 7 for the case of  $T_n = 4$  K, typical noise equivalent temperature of cryogenic HEMT amplifier<sup>12</sup>. Red and green dashed lines in figure 7 represent maximum and minimum resonance frequencies according with equation 3, while dashed-dot blue, black and cyan the minimum noise ( $P_{\text{exc}}, f_{\text{exc}}$ ) trajectories. These three trajectories describe the position followed by the optimum open-loop gains previously presented in figure 5. Colored stars are the local noise minimums at  $P_{\text{exc}} = -70$  dBm, exactly at the same positions where the maximum gains were calculated in figure 5. As we previously mentioned, only additive noise was considered. Therefore, the optimum readout parameters are valid for this condition.

As can be seen in figure 7, the noise minimums for low powers always lie within the maximum and minimum resonant frequencies and the optimum conditions for amplitude are symmetrically located on both sides of the optimum condition for the resonator's phase. In order to compare the demodulated noise values for both demodulation domains, the minimum noise levels corresponding to these trajectories were simulated again for two different additive noise temperatures. In line with new amplification technologies, we performed simulations in the Standard Quantum Limit<sup>19,43</sup> (SQL) condition with  $T_n = hf_{\text{exc}}/k_B$  together with the  $T_n = 4$  K previously used. The results are plotted together in figure 8. For these cases, flux noise levels can be estimated by using the additive noise version of equations 17 and 18,

$$\sqrt{S_{\Phi}^{\theta}} \approx \frac{1}{r} \sqrt{\frac{k_B T_n}{P_{\text{exc}}}} \left| \frac{\partial \theta}{\partial \Phi} \right|^{-1} \quad (25)$$

$$\sqrt{S_{\Phi}^{\gamma}} \approx \sqrt{\frac{k_B T_n}{P_{\text{exc}}}} \left| \frac{\partial \gamma}{\partial \Phi} \right|^{-1} \quad (26)$$

In accordance with these equations, at low power the transfer coefficients remain constant and the noise level decreases proportionally to  $\sqrt{S_{\Phi, \text{white}}} \propto 1/\sqrt{P_{\text{exc}}}$  until it reaches a plateau in which both open-loop gain values reach a level of around  $P_{\text{exc}} \approx -63$  dBm where the  $\mu\text{MUX}$  becomes insensitive to flux variations. Using  $P_{\text{exc}} = -70$  dBm, simulated optimum gain values yielded  $G_{\theta}^{\text{opt}} = 4.90 \text{ rad}/\Phi_0$  and  $G_{\gamma}^{\text{opt, up}} = G_{\gamma}^{\text{opt, low}} = 2.21/\Phi_0$  (see figure 5). Thus, for a resonance circle radius  $r \approx Q_1/2Q_c \approx 0.49$  the calculated noise values results are  $\sqrt{S_{\Phi, \text{SQL}}^{\theta}} \approx 0.071 \mu\Phi_0/\sqrt{\text{Hz}}$

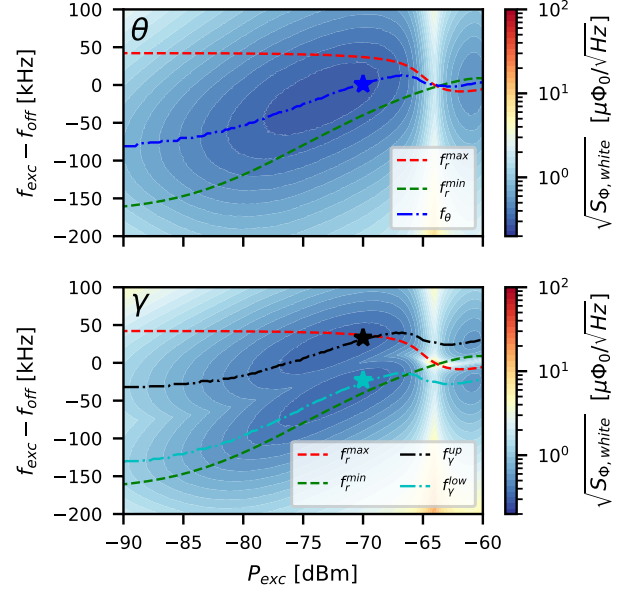


FIG. 7. Open-loop demodulated white noise flux density  $\sqrt{S_{\Phi, \text{white}}}$  for both demodulation domains as a function of probe tone frequency  $f_{\text{exc}}$  and power  $P_{\text{exc}}$  for an additive noise temperature of  $T_n = 4$  K. Green and red dashed lines represent maximum  $f_r^{\text{max}}$  and minimum  $f_r^{\text{min}}$  resonance frequencies respectively. Top) Resonator's phase demodulation, dashed-dot blue  $f_{\theta}$  line is the optimum trajectory to achieve minimum noise. Bottom) Resonator's amplitude demodulation, dashed-dot black and cyan curves are the optimum trajectories to achieve both upper  $f_{\gamma}^{\text{up}}$  and lower  $f_{\gamma}^{\text{low}}$  local minimum noise values.

and  $\sqrt{S_{\Phi, \text{SQL}}^{\gamma}} \approx 0.08 \mu\Phi_0/\sqrt{\text{Hz}}$  for the SQL, in contrast to  $\sqrt{S_{\Phi, 4K}^{\theta}} \approx 0.30 \mu\Phi_0/\sqrt{\text{Hz}}$  and  $\sqrt{S_{\Phi, 4K}^{\gamma}} \approx 0.34 \mu\Phi_0/\sqrt{\text{Hz}}$  with  $T_n = 4$  K, in well agreement with the simulations. Dotted red and grey lines represent the aforementioned noise values in the case of resonator's phase readout. Leaving aside technical difficulties that may be encountered when implementing the demodulation of one of the domains, which will be discussed in the next subsections, there is no strong argument based on noise performance to decide for either domain. This is given by the non-appreciable noise differences in the simulation results. Therefore, we will evaluate the impact of the remaining noise sources in order to find considerable differences that would indicate the existence of a preferential domain.

### 2. TLS and Multiplicative Noise Impact for Open-Loop

In order to quantify the impact of the non-additive noise sources, we performed individual simulations for each noise source under the optimum readout parameters for additive noise, represented with stars in figure 7. As mentioned earlier, Two-Level Systems noise is one of the most common noise sources and particularly important in open-loop readout due

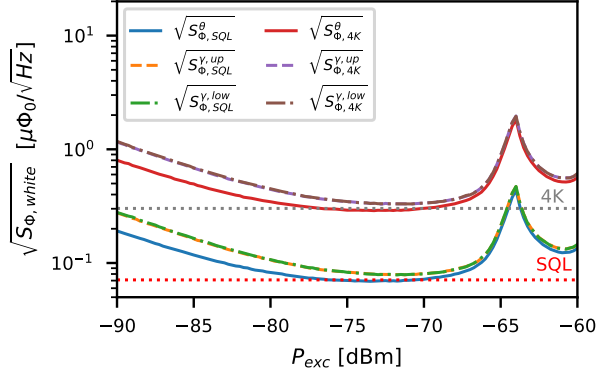


FIG. 8. Open-loop demodulated minimum white noise flux density  $\sqrt{S_{\Phi,white}}$  for every demodulation domain as a function of power  $P_{exc}$  for both SQL and  $T_n = 4$  K cases. Solid lines correspond to minimum noise for resonator's phase readout while dashed and dashed-dot lines are upper and lower local minimums for amplitude readout. Dotted grey and red lines are the minimum noise values for resonator's phase demodulation in the Standard Quantum Limit (SQL) and  $T_n = 4$  K conditions evaluated at  $P_{exc} = -70$  dBm.

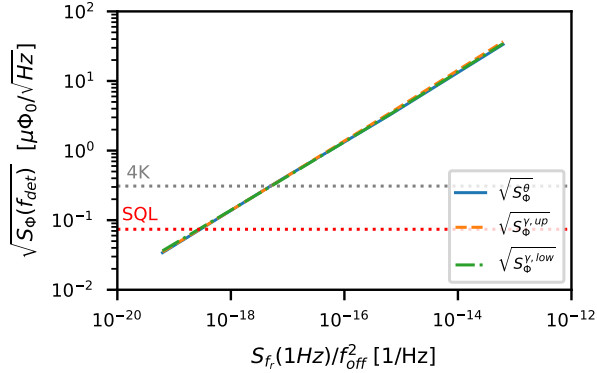


FIG. 9. Open-loop demodulated white noise flux density  $\sqrt{S_{\Phi,white}}$  as a function of the Two-Level Systems (TLS) noise level of  $S_{fr}(1\text{Hz})/f_{off}^2$  for both demodulation domains in the minimum additive noise condition for a constant  $P_{exc} = -70$  dBm. As a reference, dotted red and grey lines represent the minimum noise values for resonator's phase demodulation in the case of the Standard Quantum Limit (SQL) and  $T_n = 4$  K respectively.

to its frequency dependence<sup>34</sup>. Here, TLS noise was represented by its fractional frequency density  $S_{fr}/f_{off}^2$  with a frequency slope of  $1/f$  and taking values from  $6.25 \cdot 10^{-20} \text{ Hz}^{-1}$  to  $6.25 \cdot 10^{-14} \text{ Hz}^{-1}$  when evaluated at 1 Hz. Due to the TLS noise saturation depending on the readout power<sup>34</sup>, it is worth to mention that TLS noise is specified for  $P_{ext} = -70$  dBm. Simulations results for each domain measured at detector frequencies of  $f_{det} \approx 762$  Hz are shown in figure 9. As in the previous plots, the minimum noise values for the SQL and  $T_n = 4$  K were included as reference.

Results in figure 9 allows to set maximum TLS noise levels

of  $S_{fr}(1\text{Hz})/f_{off}^2 = 3 \cdot 10^{-18} \text{ Hz}^{-1}$  and  $S_{fr}(1\text{Hz})/f_{off}^2 = 6.6 \cdot 10^{-17} \text{ Hz}^{-1}$  for the SQL and  $T_n = 4$  K respectively avoiding the TLS as dominant noise source, but once again, showing no preferential demodulation domain.

Contrary to the TLS noise, multiplicative and additive noise sources can be compared directly in the same NSD units. Therefore, the simulations were performed as function of the NSD values for each noise source in the same conditions as before using  $P_{exc} = -70$  dBm. Equivalent noise temperatures starting from the SQL with  $T_n = hf_{exc}/k_B \approx 0.24$  K, to  $T_n = 8$  K, corresponding to NSDs from  $-135$  dBc/Hz to  $-120$  dBc/Hz were used in the case of additive noise. While for phase and amplitude readout noise, NSD going from  $-130$  dBc/Hz to  $-100$  dBc/Hz. Since both local minimums for amplitude yield the same demodulated noise for open-loop demodulation, only the upper local minimum is considered in the following analysis. The results of these simulations as a function of the NSD are shown in figure 10. As demonstrated previously, resonator's phase readout lead to a slightly lower noise than amplitude readout for the same NSD. In addition, as expected from table II, noise levels scales proportional to NSD with  $\sqrt{S_{\Phi}} \propto \sqrt{NSD}$  being additive noise the dominant noise source compared with multiplicative sources for equal NSD values. When considering non-correlated noise sources acting together, the total system noise is the quadrature summation all individual contributions. Therefore, we defined a rejection factor  $A$  for each noise source and demodulation domain equal to the NSD difference with respect to the additive NSD that would result in the same demodulated noise level. This factor is represented with a black arrow in figure 10 for the case of resonator's amplitude demodulation and is equal to the distance in NSD units between parallel dashed lines for a constant flux noise density. Thus, for amplitude demodulation there is a  $\approx 10$  dB rejection of amplitude noise. In contrast using resonator's phase demodulation, there are  $\approx 19$  dB and more than 40 dB rejection values for phase and amplitude noise respectively. Particularly, amplitude demodulation is more sensitive than phase demodulation to amplitude noise because the readout tone is positioned further away from the resonance where its projection is considerably greater compared with phase noise and the amplitude open-loop gain lower. On the contrary, resonator's phase demodulation is more sensitive to phase noise because the maximum open-loop gain requires the probe tone on resonance where phase noise projection is maximum (see figure 2).

### 3. Optimum Domain for Open-loop

Previous results suggest that maximum sensitivity is achieved in the resonator's phase domain due to the lower demodulated noise level in the additive noise case and high rejection to multiplicative noise sources compared to amplitude domain. Unfortunately, this is not a realistic scenario in the case of open-loop readout. Phase and amplitude noise spectral components (equation 11) usually grow rapidly for small frequency offsets far exceeding additive noise, impacting directly in the detector signal. As an example, in order

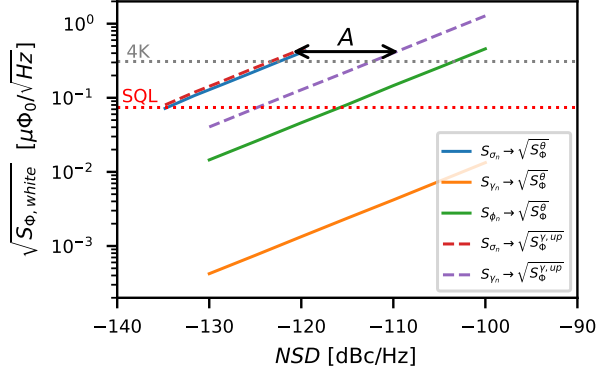


FIG. 10. Open-loop demodulated white flux noise density  $\sqrt{S_{\Phi,white}}$  for every demodulation domain as a function of the noise spectral densities (NSD) for each noise source in the minimum additive noise condition for a constant  $P_{exc} = -70$  dBm. Dashed lines correspond to resonator's amplitude domain, while solid lines are for resonator's phase readout. Grey and Red dotted lines are plotted as a reference and are equal to the white noise values for the Standard Quantum Limit (SQL) and for  $T_n = 4$  K for resonator's phase readout. As an example, black arrow represents the amplitude noise rejection factor A in amplitude domain readout.

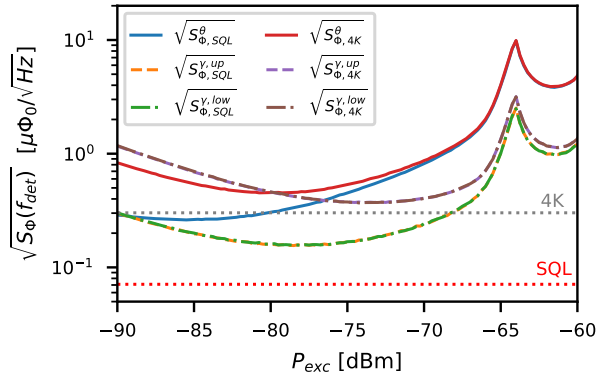


FIG. 11. Open-loop demodulated flux noise density  $\sqrt{S_{\Phi}(f_{det})}$  for every demodulation domain as a function of power  $P_{exc}$  for both SQL and  $T_n = 4$  K cases. Solid lines correspond to minimum noise for resonator's phase readout while dashed and dashed-dot lines are upper and lower local minimums for amplitude readout. Dotted grey and red lines are the minimum noise values for resonator phase demodulation in the Standard Quantum Limit (SQL) and  $T_n = 4$  K conditions evaluated at  $P_{exc} = -70$  dBm.

to determine the expected open-loop performance of a real SDR readout system<sup>36</sup>, the measured noise values shown in figure 4 were included in our simulation framework. Since the TLS noise did not show a preferential readout region and we assume a proper resonator design, it was not included in this case. The results of the demodulated noise for every domain for both SQL and  $T_n = 4$  K additive noise conditions are shown in figure 11.

Clearly, the demodulated noise is dominated by the multiplicative noise and its effect is most noticeable at high powers and near the SQL<sup>43</sup>. In the case of the resonator's phase domain it is completely dominated by the multiplicative noise values of  $S_{\phi}(f_{det}) \approx -96$  dBc/Hz and  $S_{\gamma}(f_{det}) \approx -116$  dBc/Hz for phase and amplitude respectively. Both are considerably larger than the additive noise at the detector frequency  $S_{\sigma}(f_{det})$  (see colored stars in figure 4). Noise levels at  $P_{exc} = -70$  dBm are  $\sqrt{S_{\Phi}^{\theta}(f_{det})} \approx 0.82\mu\Phi_0/\sqrt{\text{Hz}}$  and  $\sqrt{S_{\Phi}^{\gamma}(f_{det})} \approx 0.24\mu\Phi_0/\sqrt{\text{Hz}}$  for the SQL,  $\sqrt{S_{\Phi}^{\theta}(f_{det})} \approx 0.87\mu\Phi_0/\sqrt{\text{Hz}}$  and  $\sqrt{S_{\Phi}^{\gamma}(f_{det})} \approx 0.40\mu\Phi_0/\sqrt{\text{Hz}}$  for the  $T_n = 4$  K case. All of them are consistent with the values shown in figure 10 for their respective NSD levels. Based on these results and equations 25 and 26, it is possible to calculate an equivalent system temperature which reflects the measured noise. This would be the temperature that one would measure and attribute it directly to the additive noise, not knowing that it is produced by the multiplicative noise. In the case of phase noise, one would measure  $T_{sys}^{\theta,SQL} \approx 29$  K and  $T_{sys}^{\theta,4K} \approx 33$  K, as for amplitude  $T_{sys}^{\gamma,SQL} \approx 2$  K and  $T_{sys}^{\gamma,4K} \approx 5.6$  K, considerably higher than the real additive noise equivalent temperature  $T_n$ .

While phase and amplitude noise can be reduced at lower frequencies using an ultra low-noise frequency reference<sup>31</sup>, and TLS strongly reduced properly choosing resonator materials and geometry<sup>34</sup>, they are still a problem specially in the case of bolometric applications. Therefore, the FRM technique mentioned above in III D 2, can be used to mitigate these effects along with other limitations previously mentioned.

## B. Flux-Ramp Demodulation Noise Performance

Similarly to the open-loop demodulation, we replicated the noise characterization procedure of a real  $\mu\text{MUX}$  device. For the determination of the noise density in the FRD scheme described by equations 21, 20. First, we generated the modulation flux  $\varphi_{mod}[m]$  and the detector signal  $\varphi_{det}[m]$  using the parameters described in table III. Both fluxes were added,  $f_r[m]$  and the transmission parameter  $S_{21}(f_{exc}, P_{exc}, \varphi_{mod})[m]$  consequently iteratively calculated. Later, and using the circle parameters previously stored, resonator's phase  $\theta(f_{exc}, P_{exc}, \varphi)[m]$  and amplitude  $\gamma(f_{exc}, P_{exc}, \varphi_{mod})[m]$  time traces were obtained. Finally, we apply the FRD for both domains in order to get the detector signal time-traces  $\varphi_{\theta}[n]$  and  $\varphi_{\gamma}[n]$ . Here, we used  $n$  instead of  $m$  as a consequence of the decimation produced by the FRD<sup>28,40</sup> (see figure 6).

### 1. Optimum Readout Parameters for FRD

The demodulated detector time-traces  $\varphi_{det}[n]$  for both domains were calculated as a function of the frequency  $f_{exc}$  and power  $P_{exc}$  considering only additive noise with  $T_n = 4$  K. By means of the Welch's method<sup>42</sup>, the white flux noise spectral

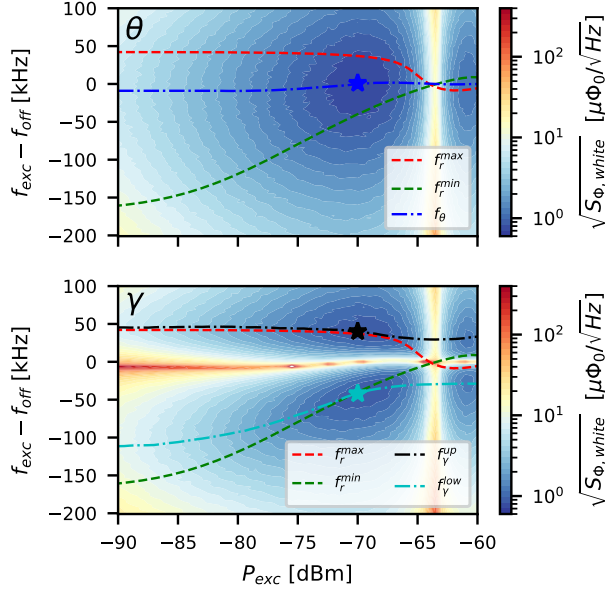


FIG. 12. Flux-ramp demodulated white flux noise density  $\sqrt{S_{\Phi,white}}$  for both demodulation domains as a function of probe tone frequency  $f_{exc}$  and power  $P_{exc}$ . Top) Resonator's phase demodulation, green and red dashed lines represent maximum  $f_r^{max}$  and minimum  $f_r^{min}$  resonance frequencies respectively. Dash-dot blue lines  $f_\theta$  is the optimum trajectory to achieve minimum noise. Bottom) Amplitude demodulation, dash-dot black and cyan curves are the optimum trajectories to achieve both upper  $f_\gamma^{up}$  and lower  $f_\gamma^{low}$  local minimum noise values. Hamming windows function with  $n_{disc} = 1$  and  $n_{\Phi_0} = 4$  were used.

density  $\sqrt{S_{\Phi,white}}$  was calculated. The results of these simulations for both domains are shown in figure 12. Red and green dashed lines represent maximum and minimum resonance frequencies, while dashed-dot blue, black and cyan the minimum noise ( $P_{exc}, f_{exc}$ ) trajectories. Colored stars are the absolute noise minima at  $P_{exc} \approx -70$  dBm for both domains.

In principle, we would assume that the noise minima will also follow the trajectories previously found for the open-loop scenario (figure 7). But this is not the case, the trajectories mainly differ, only approaching each other at high powers. This behaviour is mainly determined by the spectral components of the resonator's phase and amplitude time-traces described by their Fourier series as,

$$\theta(t) \approx \Theta_0 + \sum_{p=1}^{\infty} \Theta_p \sin(2\pi p f_{mod} t + \lambda_p) \quad (27)$$

$$\gamma(t) \approx \Gamma_0 + \sum_{p=1}^{\infty} \Gamma_p \sin(2\pi p f_{mod} t + \varepsilon_p) \quad (28)$$

Where the fundamental frequency is  $f_{mod} = n_{\Phi_0} f_{ramp}$  (also called SQUID frequency) and  $\Theta_p, \Gamma_p, \lambda_p, \varepsilon_p$  amplitude and phase spectral coefficients. Based on the FRM<sup>28</sup>, we can as-

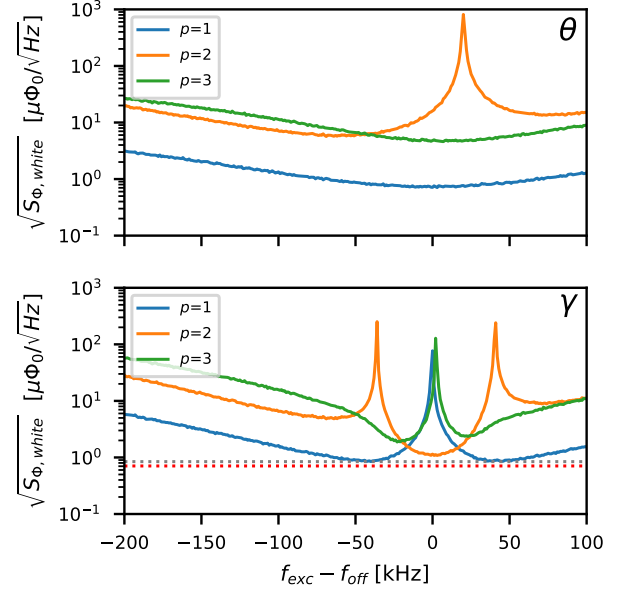


FIG. 13. Flux-ramp demodulated white flux noise density  $\sqrt{S_{\Phi,white}}$  as a function of  $f_{exc}$  for every demodulated domain and selected FRM component  $f_{dem} = p \cdot f_{mod}$  for constant  $P_{exc} = -70$  dBm and additive noise temperature of  $T_n = 4$  K. Top) Resonator's phase demodulation. Bottom) Amplitude demodulation. Red and grey lines show phase and amplitude noise minimums respectively. Hamming window functions with  $n_{disc} = 1$  and  $n_{\Phi_0} = 4$  were used.

sume that the detector signal changes the instantaneous frequency of each harmonic component  $f_{dem} = p \cdot f_{mod}$  and consequently each component is phase modulated. However, while the modulation index is given by the detector signal, the carrier power depends on the amplitude spectral components of each domain (i.e.  $\Theta_p$  and  $\Gamma_p$ ). Due to the fact that the first component is usually demodulated, noise values increase when either  $\Theta_p$  or  $\Gamma_p$  decreases. In order to probe this, we swept  $f_{exc}$  at constant power of  $P_{exc} = -70$  dBm, and the detector signal was demodulated for each harmonic component changing  $p$  in equations 20 and 21. Only one period was discarded considering that the flux-ramp transient lasts less than one period of the highest modulating frequency harmonic. The results of the simulation are shown in figure 13.

Blue traces in both panels of figure 13 correspond to the demodulation of the first harmonic component  $p = 1$ , consistent with the results of figure 12. Dotted red and grey lines are the minimum demodulated white flux noise for resonator's phase and amplitude respectively, achieved at conditions represented by the blue, black and cyan stars. Like in the open-loop scheme, resonator's phase domain gives the lowest possible noise although the difference with amplitude demodulation is not considerable. In the case of the phase, we can see that demodulated noise for the first component is always lower than the rest. On the contrary, in the case of amplitude readout, when the probe tone  $f_{exc}$  is close to the unaltered resonance frequency  $f_{off}$  noise diverges for the first and third demodulated



component while for the second there is a minimum in accordance with<sup>21</sup>. Therefore, the absolute minimum noise conditions implies the demodulation of the first harmonic at its maximum amplitude (i.e.  $\Theta_1^{max}$  and  $\Gamma_1^{max}$ ). Since the total power is spread out between harmonics, this is fulfilled when the sum of the powers of the other harmonics reach their minimums. On the other hand, for a fixed  $f_{exc}$ , the spectral components are determined by  $P_{exc}$ <sup>25</sup>. When power increases  $P_{exc}$ , both  $\beta_{eff}$  and  $\eta$  decrease, leading again to a sinusoidal response in resonator phase and amplitude, until there is no response (i.e.  $\Theta_p \approx \Gamma_p \approx 0$ ). Taking advantage of the fact that resonator's phase and amplitude behave as sinusoidal signals at high powers, equations 22 and 23 in the additive noise case can be easily calculated considering  $\theta(\Phi) \approx \Theta_1 \sin(2\pi\Phi/\Phi_0)$   $\gamma(\Phi) \approx \Gamma_1 \sin(2\pi\Phi/\Phi_0)$  yielding to<sup>19</sup>,

$$\sqrt{S_{\Phi}^{\theta}} \approx \frac{1}{r} \frac{\sqrt{2\kappa/\alpha}}{2\pi\Theta_1} \sqrt{\frac{k_B T_n}{P_{exc}}} \quad (29)$$

$$\sqrt{S_{\Phi}^{\gamma}} \approx \frac{\sqrt{2\kappa/\alpha}}{2\pi\Gamma_1} \sqrt{\frac{k_B T_n}{P_{exc}}} \quad (30)$$

With the purpose of verifying the validity of these expressions to later use them to estimate system temperature  $T_{sys}$ , first we numerically determined the amplitude of the fundamental resonator's phase and amplitude components yielding  $\Theta_1 \approx 0.63$  rad and  $\Gamma_1^{up} \approx \Gamma_1^{low} \approx 0.27$ . Second, we demodulated white flux noise for both domains as a function of probe tone frequency  $f_{exc}$  at constant power  $P_{exc} \approx -70$  dBm for three different cases: 1) Boxcar window  $w[n]$  without discarding, 2) Boxcar window and one period discarded and 3) Hamming window with one period discarded. For all cases we used  $n_{\Phi_0} = 4$  and the parameters in table III. The results presented in figure 14 for the non-discarding case were  $\sqrt{S_{\Phi}^{\theta}} \approx 0.52\mu\Phi_0/\sqrt{Hz}$  and  $\sqrt{S_{\Phi}^{\gamma}} \approx 0.62\mu\Phi_0/\sqrt{Hz}$  for phase and amplitude respectively, while in the second case  $\sqrt{S_{\Phi}^{\theta}} \approx 0.61\mu\Phi_0/\sqrt{Hz}$  and  $\sqrt{S_{\Phi}^{\gamma}} \approx 0.72\mu\Phi_0/\sqrt{Hz}$ . Lastly, using Hamming window,  $\sqrt{S_{\Phi}^{\theta}} \approx 0.71\mu\Phi_0/\sqrt{Hz}$  and  $\sqrt{S_{\Phi}^{\gamma}} \approx 0.84\mu\Phi_0/\sqrt{Hz}$ . These values are in well agreement with expressions 29 and 30 using the aforementioned  $\Theta_1$  and  $\Gamma_1$  values. As expected, discarding a period yielded a degradation of  $\sqrt{4/3} \approx 1.15$ , while the Hamming window  $\sqrt{4\kappa/3} \approx 1.35$ . This corresponds to a factor  $\kappa = 1.37$  coincident with the equivalent noise bandwidth of the Hamming window with respect to the Boxcar. Although the Hamming window improves linearity<sup>40</sup>, its main-lobe is wider compared to the boxcar window leading to an increase in the noise level. For the purpose of this work, this degradation is not important since it affects both domains equally.

Similar to the open-loop demodulation, the noise in the optimal trajectories for both domains was determined for the SQL and  $T_n = 4$  K. The results are shown in figure 15. Again, resonator's phase readout provides the best performance and noise densities decreases with  $\sqrt{S_{\Phi,white}} \propto 1/\sqrt{P_{exc}}$  for both domains reaching minimums at  $P_{exc} = -70$  dBm. Unlike the

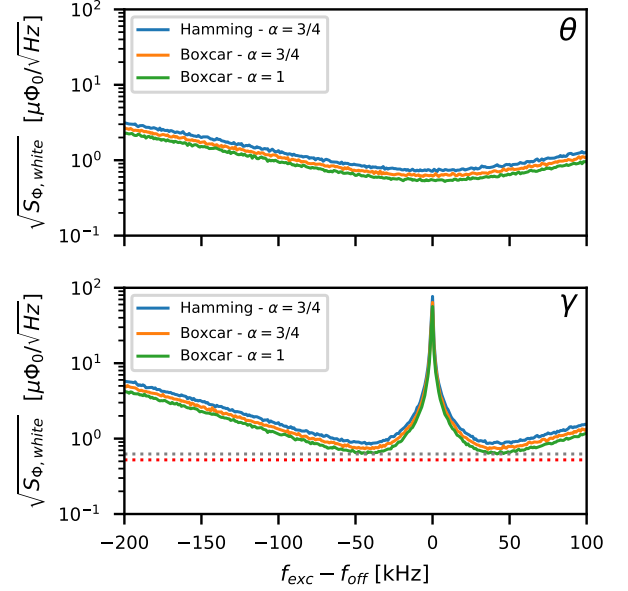


FIG. 14. Flux-ramp demodulated white flux noise density  $\sqrt{S_{\Phi,white}}$  as a function of  $f_{exc}$  for different windows functions  $w(t)$  and number of discarded periods  $n_{disc}$  with constant  $P_{exc} = -70$  dBm and additive noise temperature of  $T_n = 4$  K. Top) Resonator's phase and Bottom) Amplitude. Red and grey lines show phase and amplitude noise minimums respectively for a Boxcar window function, without periods discarded.

open-loop case, both amplitude minima differ at low powers, while at high powers they coincide due to the sinusoidal behaviour explained earlier. In agreement with equations 29 and 30 noise values in the SQL are  $\sqrt{S_{\Phi,SQL}^{\theta}} \approx 0.18\mu\Phi_0/\sqrt{Hz}$  and  $\sqrt{S_{\Phi,SQL}^{\gamma}} \approx 0.22\mu\Phi_0/\sqrt{Hz}$  being  $\sqrt{T_{4K}/T_{SQL}} \approx 4$  lower than the  $T_n = 4$  K case. As expected, these values represent a degradation of  $c_{deg}^{\theta} \approx 2.53$  and  $c_{deg}^{\gamma} \approx 2.8$  with respect to open-loop demodulation. Smaller values can be achieved removing the windows or not discarding periods depending on the linearity requirements or flux-ramp transient duration. Despite the imposed degradation, FRM provides other advantages as we will demonstrate below using our simulation framework in the following sections.

## 2. TLS and Multiplicative Noise Impact for FRD

As shown in section IV A 2, we performed simulations to evaluate the impact of both TLS noise and multiplicative readout system noise for FRD. Starting with TLS, we determined the demodulated noise  $\sqrt{S_{\Phi,white}}$  at the detector frequencies  $f_{det}$ , for the same fractional frequency densities  $S_{fr}(1Hz)/f_{off}^2$  values used before. The results are shown in figure 16 for both domains at the optimum conditions represented by stars in figure 12. It can be seen that although the noise level increased with respect to the un-modulated case, for the same

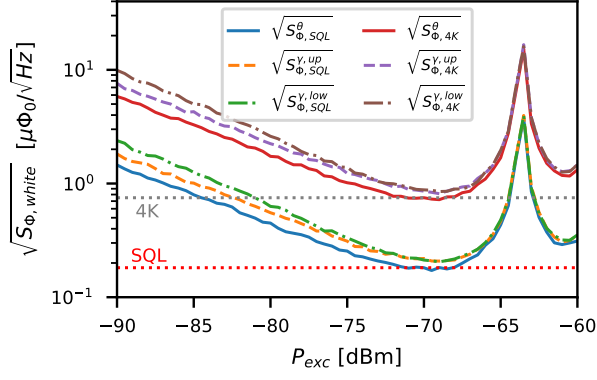


FIG. 15. Flux-ramp demodulated minimum white flux noise density  $\sqrt{S_{\Phi,white}}$  for every demodulation domain as a function of power  $P_{exc}$  and additive noise temperature of  $T_n = 4$  K. Solid lines correspond to minimum noise for resonator's phase readout while dashed and dashed-dot lines are upper and lower local minimums for amplitude readout. As a reference, dotted red and grey lines represent the minimum noise values for resonator's phase demodulation with a power of  $P_{exc} = -70$  dBm in the case of the Standard Quantum Limit (SQL) and  $T_n = 4$  K respectively. Hamming window functions with  $n_{disc} = 1$  and  $n_{\Phi_0} = 4$  were used.

noise density TLS noise represents a lower impact with respect to the additive noise levels represented by the red and grey dotted lines. This is due to demodulation process that down-converts the information signal from the carrier frequency  $f_{mod} \approx 61$  kHz, and therefore the noise evaluated at the same frequency  $S_{fr}(f_{mod})/f_{off}^2$ . This value is considerably lower than the value at  $S_{fr}(f_{det})/f_{off}^2$  due to the  $1/f$  TLS dependency. Therefore, relaxing the maximum TLS noise requirements to  $S_{fr}(1\text{Hz})/f_{off}^2 = 2 \cdot 10^{-17}$  Hz $^{-1}$  and  $S_{fr}(1\text{Hz})/f_{off}^2 = 4 \cdot 10^{-16}$  Hz $^{-1}$  for the SQL and  $T_n = 4$  K respectively. As far as the readout domain is concerned, results show again no preference for resonator phase or amplitude demodulation at higher powers, leaving multiplicative noise the main factor to decide if there is an optimal readout domain.

Demodulated noise results for multiplicative sources under the optimum readout condition for additive noise found in section IV B 1 as a function of NSD are shown in figure 17. As seen in previous results, resonator's phase domain is the optimal domain for the additive noise case while the other noise sources remain negligible for the same NSD values. All noise demodulated values increase with respect to the open-loop case, following the same dependence with  $\sqrt{S_{\Phi}} \propto \sqrt{NSD}$ . However, all previously defined rejection factors decreased from 10 dB to 8 dB for amplitude noise in the amplitude domain, while for the resonator's phase demodulation from 19 dB to 18 dB and from 40 dB to 14 dB for phase and amplitude noise respectively. As expected, all rejection factors decreased as a consequence of the FRM. Particularly, phase demodulation became more sensitive to amplitude noise when the readout tone is positioned further away from the resonance, where its projection is considerably greater and the gain lower. On the contrary, phase noise in these positions is

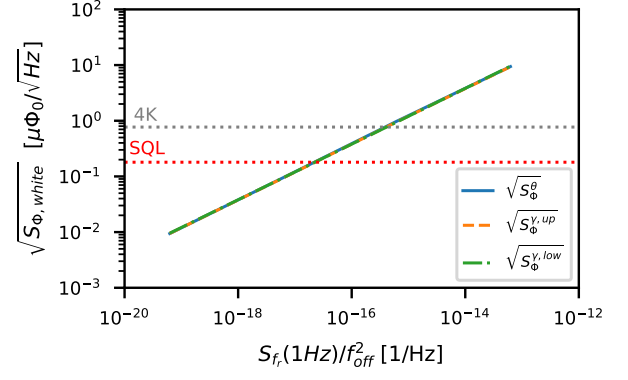


FIG. 16. Flux-ramp demodulated white flux noise density  $\sqrt{S_{\Phi,white}}$  as a function of the Two-Level Systems (TLS) noise level of  $S_{fr}/f_{off}$  for both demodulation domains in the minimum additive noise condition for a constant  $P_{exc} = -70$  dBm. As a reference, dotted red and grey lines represent the minimum noise values for phase demodulation with a power of  $P_{exc} = -70$  dBm in the case of the Standard Quantum Limit (SQL) and  $T_n = 4$  K respectively. Hamming window function with  $n_{disc} = 1$  and  $n_{\Phi_0} = 4$  were used ( $\alpha = 4/3$ ).

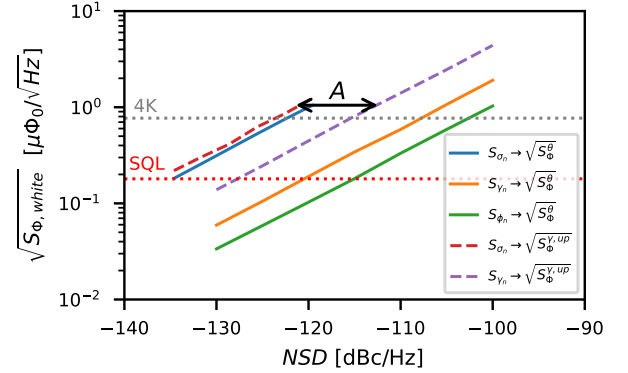


FIG. 17. Flux-ramp demodulated white flux noise density for every demodulation domain and power for additive noise with 4K. As a reference, dotted red and grey lines represent the minimum noise values for phase demodulation with a power of  $P_{exc} = -70$  dBm in the case of the Standard Quantum Limit (SQL) and  $T_n = 4$  K respectively. Hamming window functions with  $n_{disc} = 1$  and  $n_{\Phi_0} = 4$  were used. As an example, black arrow represents the amplitude noise rejection factor  $A$  in amplitude domain readout.

lower, therefore it has less impact. However, as we demonstrated before, system noise depends on the characteristics of the readout hardware used.

### 3. Optimum Domain for FRD

Similar to the open-loop demodulation case, we used the simulation framework in order to predict the system noise performance of the SDR system used as an example. Measured



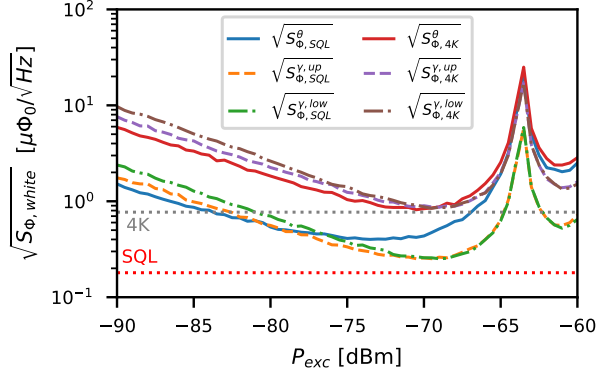


FIG. 18. Flux-ramp demodulated white flux noise density  $\sqrt{S_{\Phi,white}}$  for every demodulation domain as a function of power  $P_{exc}$  and additive noise temperature of  $T_n = 4$  K. As a reference, dotted red and grey lines represent the minimum noise values for phase demodulation with a power of  $P_{exc} = -70$  dBm in the case of the Standard Quantum Limit (SQL) and  $T_n = 4$  K respectively. Hamming window functions with  $n_{disc} = 1$  and  $n_{\Phi_0} = 4$  were used.

noise values shown in figure 4 using magenta and cyan triangles were included in our simulation framework and again, TLS noise was not considered. The results of the flux-ramp demodulated noise for every domain and both SQL and  $T_n = 4$  K additive noise conditions are shown in figure 18. Once again, amplitude readout shows the best performance when a real SDR readout system is used, and the impact of multiplicative noise became more relevant for the SQL scenario. In the case of the resonator phase domain it is completely dominated by the phase noise of the readout system which has a value of  $S_{\phi}(f_{mod}) \approx -108$  dBc/Hz at the frequency  $f_{mod}$ . Amplitude noise at the same frequency with  $S_{\gamma}(f_{mod}) \approx -130$  dBc/Hz does not have NSD to represent a considerable degradation for any of both scenarios. Clearly, like TLS, FRM helped on reducing the low-frequency multiplicative noise compared to the open-loop scheme. Quantitatively, noise levels at  $P_{exc} = -70$  dBm are  $\sqrt{S_{\Phi}^{\theta}} \approx 0.43 \mu\Phi_0/\sqrt{Hz}$  and  $\sqrt{S_{\Phi}^{\gamma}} \approx 0.26 \mu\Phi_0/\sqrt{Hz}$  for the SQL and  $\sqrt{S_{\Phi}^{\theta}} \approx 0.84 \mu\Phi_0/\sqrt{Hz}$  and  $\sqrt{S_{\Phi}^{\gamma}} \approx 0.90 \mu\Phi_0/\sqrt{Hz}$  for the  $T_n = 4$  K case, all of them consistent with the values shown in figure 17 for their respective NSD levels. Using these results and equations 29 and 30, it is also possible to calculate an additive equivalent system temperature. In the resonator's phase demodulation case would be measure  $T_{sys}^{\theta,SQL} \approx 1.4$  K and  $T_{sys}^{\theta,4K} \approx 5.1$  K, as for amplitude  $T_{sys}^{\gamma,SQL} \approx 0.4$  K and  $T_{sys}^{\gamma,4K} \approx 4.5$  K. Where only in the SQL case multiplicative noise represents considerably higher system temperature  $T_{sys}$  than the additive temperature  $T_n$ .

## V. DISCUSSION

Previous simulations contributed to improve system noise estimations finding the maximum noise values that can be managed for a given sensitivity. Thus enabling the optimization of the associated  $\mu$ MUX, cold and warm-temperature readout systems. Although for this work the criterion for the selection of optimal parameters was found to be based on the condition of minimum readout noise, two important factors must be taken into account. First, for a large number of channels  $N$ , the total power at the output of the  $\mu$ MUX grows with  $P_{out} \propto N$  and can saturate the HEMT amplifier degrading the noise performance<sup>12</sup>. Particularly in the case presented in IV B 1 there is no substantial difference, the resonator's phase demodulation presented  $P_{out} \approx -82$  dBm with respect to the amplitude with  $P_{out} \approx -79$  dBm for a  $P_{exc} = -70$  dBm. Second, while the phase demodulation yielded better results for the additive noise case, the amplitude is robust to other types of noise, as well as not requiring a resonance circle transformation which can be affected by phase variations<sup>29</sup> of the RF components and requires more digital resources to be implemented<sup>37,39</sup>.

## VI. CONCLUSION

We successfully extended the capabilities of previously developed simulation frameworks for  $\mu$ MUX readout including multiplicative noise sources, as well as the ability of demodulating data in different domains. Through different simulations the optimum readout parameters to achieve the lowest possible readout noise for a  $\mu$ MUX device optimized for bolometric applications were found in both open-loop and flux-ramp demodulation schemes. We probe that the optimal readout parameters in the case of open-loop and flux-ramp demodulation are different and mainly determined by the first harmonic component used for demodulation. We demonstrate that the dominant noise source in both cases is the additive noise and the optimal demodulation domain for this condition is the resonator's phase. Under the minimum noise parameters for additive noise, the impact of the multiplicative sources was assessed. An example using a typical SDR readout system was presented and the impact on the system noise estimated. Due to the higher readout phase noise, the results showed considerable degradation of the system noise when demodulation is performed in the phase domain. Contrarily, demodulation in amplitude yielded the minimum noise dominated by additive noise. As expected, degradation becomes more evident close to the SQL when parametric amplifiers are used. Additionally and as an integral part of this work, the performance of the flux-ramp demodulation using different windows, the effect of discarding periods, as well as the demodulation of different harmonic components was evaluated and contrasted with the open-loop case. Last but not least, it is important to note that the noise analysis of the readout system presented here is not only useful for the design of SDR readout for  $\mu$ MUX systems, but also for different frequency domain multiplexed superconducting devices such as MKIDs and QUBITS.

## DATA AVAILABILITY STATEMENT

The data and artwork that support the findings of this study are available from the corresponding author upon reasonable request.

## ACKNOWLEDGMENTS

M. E. García Redondo is supported by the Comisión Nacional de Energía Atómica (CNEA) as well as for the Helmholtz International Research School in Astroparticles and Enabling Technologies (HIRSAP). M. E. García Redondo also acknowledges the support of the Karlsruhe School of Elementary and Astroparticle Physics: Science and Technology (KSETA).

## Appendix A: Noise Projections

Considering that noise amplitudes are considerably small respect to  $S_{21}(t)$  variations, each noise source can be geometrically projected into the corresponding domain. Figure 19 shows a detailed description of figure 2. Defining the readout and resonator's phases as,

$$\phi(f_{exc}, \varphi) = \arctan \left\{ \frac{\text{Im}[S_{21}(f_{exc}, \varphi)]}{\text{Re}[S_{21}(f_{exc}, \varphi)]} \right\} \quad (\text{A1})$$

$$\theta(f_{exc}, \varphi) = \arctan \left\{ \frac{\text{Im}[S_{21}(f_{exc}, \varphi)]}{x_c - \text{Re}[S_{21}(f_{exc}, \varphi)]} \right\} \quad (\text{A2})$$

Using triangles proprieties we easily demonstrate that  $\psi = \pi/2 - \varepsilon = \theta + \phi$ , Therefore, using the adequate trigonometric relations we can write the projections of amplitude  $\gamma_n(t)$  and phase  $\phi_n(t)$  readout noise into the resonator's phase  $\theta(t)$  as follows,

$$\theta_n^{\gamma}(t) \approx \gamma_n(t) \cos(\varepsilon) = \gamma_n(t) \frac{\gamma}{r} \sin(\theta + \phi) \quad (\text{A3})$$

$$\theta_n^{\phi}(t) \approx \phi_n(t) \cos(\psi) = \phi_n(t) \frac{\gamma}{r} \cos(\theta + \phi) \quad (\text{A4})$$

Where the approximation  $\theta \approx 1/r$  was used to convert absolute voltage variations into phase units.  $r$  stands for resonance circle radius. The noise spectral densities in table II were calculated considering that, for a given scaling factor  $g$  applied to signal  $y(t)$ , the resulting power spectral density of the scaled signal  $z(t)$  is equal to  $S_z(\Delta f) = g^2 S_y(\Delta f)$ .

<sup>1</sup>S. Walker and others., "Demonstration of 220/280 ghz multichroic feedhorn-coupled tes polarimeter," *Journal of Low Temperature Physics* **199**, 891–897 (2020).

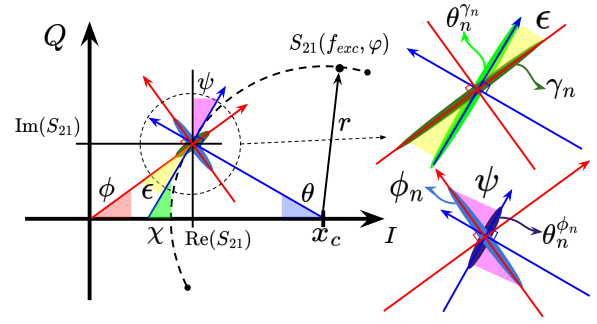


FIG. 19. Detailed description of the projections of each noise source for both demodulation domains. Amplitude  $\gamma$  and phase  $\theta$  measured form the resonator rotating frame.

- <sup>2</sup>L. Fleischmann, M. Linck, A. Burck, C. Domesle, S. Kempf, M. Rodrigues, A. Pabinger, C. Pies, J.-P. Porst, H. Rotzinger, S. Schäfer, R. Weldle, A. Fleischmann, C. Enss, and G. M. Seidel, "Physics and applications of metallic magnetic calorimeters for particle detection," *Journal of Physics: Conference Series* **150**, 012013 (2009).
- <sup>3</sup>J. Zmuidzinas, "Superconducting microresonators: Physics and applications," *Annual Review of Condensed Matter Physics* **3**, 169–214 (2012).
- <sup>4</sup>M. Piat, et al., "Qubic: Using nbsi tess with a bolometric interferometer to characterize the polarization of the cmb," *Journal of Low Temperature Physics* **200**, 363–373 (2020).
- <sup>5</sup>J. N. Ullom and D. A. Bennett, "Review of superconducting transition-edge sensors for x-ray and gamma-ray spectroscopy," *Superconductor Science and Technology* **28**, 084003 (2015).
- <sup>6</sup>L. Gastaldo et al., "The electron capture in 163ho experiment – echo," *The European Physical Journal Special Topics* **226**, 1623–1694 (2017).
- <sup>7</sup>S. M. Duff, J. Ausermann, J. A. Beall, D. Becker, R. Datta, P. A. Gallardo, S. W. Henderson, et al., "Advanced actpol multichroic polarimeter array fabrication process for 150 mm wafers," *Journal of Low Temperature Physics* **184**, 634–641 (2016).
- <sup>8</sup>M. H. Abitbol, Z. Ahmed, and others., "Cmb-s4 technology book, first edition," (2017).
- <sup>9</sup>K. D. Irwin and K. W. Lehnert, "Microwave squid multiplexer," *Applied Physics Letters* **85**, 2107–2109 (2004).
- <sup>10</sup>J. Mates, *The Microwave SQUID Multiplexer*, Ph.D. thesis, University of Colorado (2011).
- <sup>11</sup>B. Dober, Z. Ahmed, and others., "A microwave squid multiplexer optimized for bolometric applications," (2020), 10.1063/5.0033416.
- <sup>12</sup>M. Sathyanarayana Rao and others., "Simons Observatory Microwave SQUID Multiplexing Readout - Cryogenic RF Amplifier and Coaxial Chain Design," *J. Low. Temp. Phys.* **199**, 807–816 (2020), arXiv:2003.08949 [astro-ph.IM].
- <sup>13</sup>R. Gartmann, N. Karcher, R. Gebauer, O. Krömer, and O. Sander, "Progress of the echo sdr readout hardware for multiplexed mmcs," *Journal of Low Temperature Physics* **209**, 726–733 (2022).
- <sup>14</sup>C. Yu, Z. Ahmed, J. C. Frisch, and others., "SLAC microresonator RF (SMuRF) electronics: A tone-tracking readout system for superconducting microwave resonator arrays," *Review of Scientific Instruments* **94**, 014712 (2023), [https://pubs.aip.org/aip/rsi/article-pdf/doi/10.1063/5.0125084/16713259/014712\\_1\\_online.pdf](https://pubs.aip.org/aip/rsi/article-pdf/doi/10.1063/5.0125084/16713259/014712_1_online.pdf).
- <sup>15</sup>M. E. G. Redondo, T. Muscheid, R. Gartmann, J. M. Salum, L. P. Ferreyro, N. A. Müller, J. D. Bonilla-Neira, J. M. Geria, J. J. Bonaparte, A. Almela, L. E. Ardila-Perez, M. R. Hampel, A. E. Fuster, M. Platino, O. Sander, M. Weber, and A. Etchegoyen, "Rfsoic gen3-based software-defined radio characterization for the readout system of low-temperature bolometers," (2023), arXiv:2311.03480 [astro-ph.IM].
- <sup>16</sup>S. Kempf, M. Wegner, A. Fleischmann, L. Gastaldo, F. Herrmann, M. Papst, D. Richter, and C. Enss, "Demonstration of a scalable frequency-domain readout of metallic magnetic calorimeters by means of a microwave squid multiplexer," *AIP Advances* **7**, 015007 (2017).

- <sup>17</sup>J. M. Geria, M. R. Hampel, S. Kempf, J. J. Bonaparte, L. P. Ferreyro, M. E. G. Redondo, D. A. Almela, J. M. Salum, N. Müller, J. D. Bonilla-Neira, A. E. Fuster, M. Platino, and A. Etchegoyen, "Suitability of magnetic microbolometers based on paramagnetic temperature sensors for cmb polarization measurements," *Journal of Astronomical Telescopes, Instruments, and Systems* **9** (2022), 10.1117/1.JATIS.9.1.016002.
- <sup>18</sup>N. Zobrist, B. H. Eom, P. Day, B. A. Mazin, S. R. Meeker, B. Bumble, H. G. LeDuc, G. Coiffard, P. Szypryt, N. Fruitwala, I. Liparito, and C. Bockstiegel, "Wide-band parametric amplifier readout and resolution of optical microwave kinetic inductance detectors," *Applied Physics Letters* **115**, 042601 (2019), [https://pubs.aip.org/aip/apl/article-pdf/doi/10.1063/1.5098469/14525680/042601\\_1\\_online.pdf](https://pubs.aip.org/aip/apl/article-pdf/doi/10.1063/1.5098469/14525680/042601_1_online.pdf).
- <sup>19</sup>M. Malnou, J. A. B. Mates, M. R. Vissers, L. R. Vale, D. R. Schmidt, D. A. Bennett, J. Gao, and J. N. Ullom, "Improved microwave SQUID multiplexer readout using a kinetic-inductance traveling-wave parametric amplifier," *Applied Physics Letters* **122**, 214001 (2023), [https://pubs.aip.org/aip/apl/article-pdf/doi/10.1063/5.0149646/17832018/214001\\_1\\_5.0149646.pdf](https://pubs.aip.org/aip/apl/article-pdf/doi/10.1063/5.0149646/17832018/214001_1_5.0149646.pdf).
- <sup>20</sup>C. Yu, Z. Ahmed, J. M. D'Ewart, J. C. Frisch, S. W. Henderson, and M. Silva-Feaver, "A simulation suite for readout with SMuRF tone-tracking electronics," in *Millimeter, Submillimeter, and Far-Infrared Detectors and Instrumentation for Astronomy XI*, Vol. 12190, edited by J. Zmuidzinas and J.-R. Gao, International Society for Optics and Photonics (SPIE, 2022) p. 121900V.
- <sup>21</sup>C. Schuster, M. Wegner, and S. Kempf, "Simulation framework for microwave SQUID multiplexer optimization," *Journal of Applied Physics* **133**, 044503 (2023), [https://pubs.aip.org/aip/jap/article-pdf/doi/10.1063/5.0135124/17993969/044503\\_1\\_5.0135124.pdf](https://pubs.aip.org/aip/jap/article-pdf/doi/10.1063/5.0135124/17993969/044503_1_5.0135124.pdf).
- <sup>22</sup>J. van Rantwijk, M. Grim, D. van Loon, S. Yates, A. Baryshev, and J. Baselmans, "Multiplexed readout for 1000-pixel arrays of microwave kinetic inductance detectors," *IEEE Transactions on Microwave Theory and Techniques* **64**, 1876–1883 (2016).
- <sup>23</sup>J. Herrmann and others., "Frequency Up-Conversion Schemes for Controlling Superconducting Qubits," (2022), arXiv:2210.02513 [quant-ph].
- <sup>24</sup>C. Ding *et al.*, "Experimental advances with the qick (quantum instrumentation control kit) for superconducting quantum hardware," *Phys. Rev. Res.* **6**, 013305 (2024).
- <sup>25</sup>M. Wegner, C. Enss, and S. Kempf, "Analytical model of the readout power and squid hysteresis parameter dependence of the resonator characteristics of microwave squid multiplexers," *Superconductor Science and Technology* **35**, 075011 (2022).
- <sup>26</sup>F. K. Ahrens, *Cryogenic read-out system and resonator optimisation for the microwave SQUID multiplexer within the ECHO experiment*, Ph.D. thesis, Heidelberg University (2022).
- <sup>27</sup>S. Probst, F. Song, P. Bushev, A. Ustinov, and M. Weides, "Efficient and robust analysis of complex scattering data under noise in microwave resonators," *The Review of scientific instruments* **86** (2014), 10.1063/1.4907935.
- <sup>28</sup>J. A. B. Mates, K. D. Irwin, L. R. Vale, G. C. Hilton, J. Gao, and K. W. Lehnert, "Flux-ramp modulation for squid multiplexing," *Journal of Low Temperature Physics* **167**, 707–712 (2012).
- <sup>29</sup>M. Silva-Feaver, Z. Ahmed, and others., "Phase drift monitoring for tone tracking readout of superconducting microwave resonators," (2022), 10.48550/arxiv.2208.02854.
- <sup>30</sup>J. M. Salum, M. E. García Redondo, L. P. Ferreyro, J. Bonilla-Neira, N. Müller, J. M. Geria, J. Bonaparte, T. Muscheid, R. Gartmann, A. Fuster, A. Almela, M. R. Hampel, L. E. Ardila-Perez, O. Sander, S. Kempf, M. Platino, M. Weber, and A. Etchegoyen, "Spectral engineering for optimal signal performance in the microwave squid multiplexer," *Journal of Low Temperature Physics* **214** (2024), 10.1007/s10909-024-03049-6.
- <sup>31</sup>E. Rubiola, *Phase Noise and Frequency Stability in Oscillators*, The Cambridge RF and Microwave Engineering Series (Cambridge University Press, 2008).
- <sup>32</sup>*White paper: Understanding phase noise measurement techniques*, Rohde & Schwarz GmbH & Co. KG (2021).
- <sup>33</sup>*White paper: Understanding phase noise fundamentals*, Rohde & Schwarz GmbH & Co. KG (2021), version 01.01.
- <sup>34</sup>J. Gao, B. A. Mazin, P. K. Day, J. Zmuidzinas, and H. G. LeDuc, "Noise properties of superconducting coplanar waveguide microwave resonators," (2006), 10.1063/1.2711770.
- <sup>35</sup>S. Kumar and others., "Temperature dependence of the frequency and noise of superconducting coplanar waveguide resonators," *Applied Physics Letters* **92**, 123503 (2008), [https://pubs.aip.org/aip/apl/article-pdf/doi/10.1063/1.2894584/14388822/123503\\_1\\_online.pdf](https://pubs.aip.org/aip/apl/article-pdf/doi/10.1063/1.2894584/14388822/123503_1_online.pdf).
- <sup>36</sup>AMD, "Zcu216 evaluation board user guide (ug1390)," (2022).
- <sup>37</sup>J. D. Gard, D. T. Becker, D. A. Bennett, J. W. Fowler, G. C. Hilton, J. A. B. Mates, C. D. Reintsema, D. R. Schmidt, D. S. Swetz, and J. N. Ullom, "A scalable readout for microwave squid multiplexing of transition-edge sensors," *Journal of Low Temperature Physics* **193**, 485–497 (2018).
- <sup>38</sup>D. Becker, D. Bennett, M. Biasotti, M. Borghesi, *et al.*, "Working principle and demonstrator of microwave-multiplexing for the holmes experiment microcalorimeters," *Journal of Instrumentation* **14**, P10035 (2019).
- <sup>39</sup>N. Karcher, T. Muscheid, T. Wolber, D. Richter, C. Enss, S. Kempf, and O. Sander, "Online demodulation and trigger for flux-ramp modulated squid signals," *Journal of Low Temperature Physics* **209**, 581–588 (2022).
- <sup>40</sup>J. M. Salum, T. Muscheid, A. Fuster, M. E. Garcia Redondo, M. R. Hampel, L. P. Ferreyro, J. M. Geria, J. Bonilla-Neira, N. Müller, J. Bonaparte, A. Almela, L. E. Ardila-Perez, M. Platino, O. Sander, and M. Weber, "Aliasing effect on flux ramp demodulation: Nonlinearity in the microwave squid multiplexer," *Journal of Low Temperature Physics* **213**, 223–236 (2023), 54.12.02; LK 01.
- <sup>41</sup>L. P. Ferreyro, M. G. Redondo, M. R. Hampel, A. Almela, A. Fuster, J. Salum, J. M. Geria, J. Bonaparte, J. Bonilla-Neira, N. Müller, N. Karcher, O. Sander, M. Platino, and A. Etchegoyen, "An implementation of a channelizer based on a goertzel filter bank for the read-out of cryogenic sensors," (2023).
- <sup>42</sup>P. Welch, "The use of fast Fourier transform for the estimation of power spectra: A method based on time averaging over short, modified periodograms," *IEEE Trans. Audio Electroacoust.* **15**, 70–73 (1967).
- <sup>43</sup>C. M. Caves, "Quantum limits on noise in linear amplifiers," *Phys. Rev. D* **26**, 1817–1839 (1982).
- <sup>44</sup>O. Sander, N. Karcher, O. Krömer, S. Kempf, M. Wegner, C. Enss, and M. Weber, "Software-defined radio readout system for the echo experiment," *IEEE Transactions on Nuclear Science* **66**, 1204–1209 (2019).
- <sup>45</sup>C. Yu *et al.*, "Bandwidth and Aliasing in the Microwave SQUID Multiplexer," *J. Low Temp. Phys.* **209**, 589–597 (2022), arXiv:2206.09066 [physics.ins-det].